




Review: Multi-principal element alloys by additive manufacturing

Chenze Li¹, Michael Ferry², Jamie J. Kruzic¹, and Xiaopeng Li^{1,*} 

¹School of Mechanical and Manufacturing Engineering, The University of New South Wales (UNSW Sydney), Sydney, NSW 2052, Australia

²School of Materials Science and Engineering, The University of New South Wales (UNSW Sydney), Sydney, NSW 2052, Australia

Received: 20 November 2021

Accepted: 28 January 2022

Published online:
24 February 2022

© The Author(s) 2022

ABSTRACT

Multi-principal element alloys (MPEAs) have attracted rapidly growing attention from both research institutions and industry due to their unique microstructures and outstanding physical and chemical properties. However, the fabrication of MPEAs with desired microstructures and properties using conventional manufacturing techniques (e.g., casting) is still challenging. With the recent emergence of additive manufacturing (AM) techniques, the fabrication of MPEAs with locally tailorable microstructures and excellent mechanical properties has become possible. Therefore, it is of paramount importance to understand the key aspects of the AM processes that influence the microstructural features of AM fabricated MPEAs including porosity, anisotropy, and heterogeneity, as well as the corresponding impact on the properties. As such, this review will first present the state-of-the-art in existing AM techniques to process MPEAs. This is followed by a discussion of the microstructural features, mechanisms of microstructural evolution, and the mechanical properties of the AM fabricated MPEAs. Finally, the current challenges and future research directions are summarized with the aim to promote the further development and implementation of AM for processing MPEAs for future industrial applications.

Introduction

Multi-principal element alloys (MPEAs) were first reported independently by Cantor [1] and Yeh [2] in 2004 and generally contain three to five main metallic

elements with equiatomic ratio which differs from traditional alloys, whereby one or two elements dominate. Since more elements would increase the entropy of mixing of the alloy system, MPEAs are also known as high/medium entropy alloys [3]. MPEAs tend to form simple solid solutions rather

Handling Editor: M. Grant Norton.

Address correspondence to E-mail: xiaopeng.li@unsw.edu.au

than intermetallic compounds, which gives rise to their excellent mechanical properties and good thermal stability [4, 5].

MPEAs have recently enjoyed a rapid development with a clear focus on the design of new alloy systems for potential applications in various industries, such as turbine blades, thermal spray bond coatings, high-temperature molds and dies, radiation-damage resistant materials, and renewable energy industry [6–14]. The earliest and most intensely investigated alloy systems are 3d transition metal MPEAs, which are based on the elements Cr, Co, Ni, Fe, Mn, V, and Cu. Features of these MPEAs include their relatively easy formation of a simple solid solution and excellent mechanical performance and radiation resistance. The first 3d transition metal MPEA has the equiatomic composition CrCoNiFeMn and is known as the Cantor alloy [1]. In addition, Wu et al. synthesized a series of binary, ternary, and quaternary MPEAs which are subsets of the Cantor alloy with the same single FCC phase and excellent cryogenic temperature mechanical properties [15–17]. It is also worth noting that numerous studies on 3d transition metal MPEAs contain the element Al as an additive or principal element. The underlying reason is that Al plays a key role in grain refinement, in suppressing intermetallic compound formation, and in facilitating phase transition from FCC to FCC + BCC then to total BCC [18–20]. Another important MPEA system is refractory metal MPEAs system with high strength and melting temperature (more than 1800 °C) containing elements Cr, Hf, Mo, Nb, Ta, Ti, V, W with single BCC phase or BCC + Laves/B2 phase [21, 22]. For instance, Senkov et al. fabricated equiatomic NbMoTaW and VNbMoTaW MPEAs with single BCC phase structure using vacuum arc melting and both MPEAs show high yield strength at high temperature (405 MPa and 477 MPa at 1600 °C, respectively) [23]. Moreover, low-density MPEAs based on light elements Al, Li, Mg, Si, Sn, and Ti also have promising potential applications in aerospace and transportation industries. Khaled et al. designed and produced $\text{Al}_{20}\text{Li}_{20}\text{Mg}_{10}\text{Sc}_{20}\text{Ti}_{30}$ by mechanical alloying, combining both low density (2.67 g/cm^3) and high microhardness (5.9 GPa) [24].

Since MPEAs have generated substantial research interest, various manufacturing techniques for processing MPEAs have been developed in the past decades. Arc melting and mechanical alloying are the two main manufacturing techniques for MPEAs

[25–27]. Arc melting is the earliest and most widely used method for processing these alloys, which consists of several steps including first mixing different metals with a fixed ratio in a crucible and then melting the mixed metals by electrode discharge arc heating with argon as protective atmosphere, followed by casting into a mold. As the most popular manufacturing technique for MPEAs, arc melting can remove the volatile impurities (e.g., C, N, O, Si, Sn, Sb, Pb) due to its extremely high working temperature of over 3000 °C. However, arc melting also suffers some disadvantages in terms of processing MPEAs such as restricted production geometry, composition segregation, defects and large inner stress, which greatly impedes its further development and application in processing MPEAs [28]. Meanwhile, mechanical alloying is used mainly for MPEA powder production [29]. This process generally involves a mixture of different composition powders undergoing a repeated fracture and rewelding process in a high energy ball-mill machine until uniform composition is achieved in a fine MPEA powder. Mechanical alloying can be readily used for developing a wide range of MPEAs with relatively low cost and high yield. However, since the product of mechanical alloying is only MPEA powder itself, other manufacturing techniques such as hot isostatic pressing and spark plasma sintering are required for producing practically usable MPEAs parts. Additionally, the grinding media and atmosphere in the ball-mill machine will tend to contaminate the raw MPEA powder.

Additive manufacturing (AM), also known as three-dimensional (3D) printing, is regarded as a transformative and promising technology in many industries [30–32]. AM applies novel incremental manufacturing techniques under computer guidance to form a product using layer-by-layer consolidation [33, 34]. With the recent advent and rapid development of AM, there have been demonstrated advantages in processing various metals and alloys including Al, Ti, steel, shape memory alloys, metallic glasses, and MPEAs, particularly for manufacturing complex geometry components with locally tailorable microstructure and properties [35–41].

The purpose of this review article is to present the state-of-the-art in AM techniques for MPEAs, highlighting the microstructures produced, their evolution mechanisms, and the associated mechanical properties. To conclude, some current challenges and

future research directions are proposed with the aim to promote the further development and implementation of AM of MPEAs.

Additive manufacturing for multi-principal element alloys

The focus of this review article will be on two different additive manufacturing (AM) techniques which represent the large majority of studies on the fabrication of MPEAs, namely powder bed fusion (PBF) and directed energy deposition (DED) [42, 43].

Classifications of AM technologies for MPEAs

Powder bed fusion (PBF)

PBF is an emerging and widely used AM technology to selectively melt layers of metal powders using laser or electron beam as energy sources following the scanning paths predefined by a computer-aided design model [44]. The PBF process includes several steps. Firstly, software slices a 3D computer-aided design model into discrete layers and programs the scanning paths and strategy. Secondly, the machine selectively melts each successive layer of powder while the un-melted powder remains loose or partially loose on the substrate as support. Thirdly, the build platform descends by one layer thickness and the recoater spreads another layer of metal powder on top of the previous layer for subsequent scanning and melting. Depending on the energy sources for melting metal powders, PBF can be categorized into laser-powder bed fusion (LPBF) and electron beam powder bed fusion (EPBF). LPBF shows a higher cooling rate, which is up to 10^7 K/s, than EPBF, which has a typical range from 10^3 to 10^5 K/s [45]. The lower cooling rate and lower temperature gradient caused by preheating the powder bed during EPBF tends to decrease residual stresses and cracking compared to LPBF [46–48]. CrCoNiFe was the earliest MPEA investigated by PBF technology and confirmed the feasibility to fabricate MPEAs by AM [49, 50]. In addition, MPEAs with Al additions were widely researched recently using PBF and their defect phase formation mechanisms have attracted a great deal of research interest [51–54]. Additionally, refractory MPEAs, which are difficult to process due

to their low ductility and high strength at room temperature, were also successfully fabricated by PBF [55, 56].

The key adjustable processing parameters for PBF include power of the energy sources (e.g., laser power in LPBF, voltage and current controlled power in EBM), hatch spacing, scanning speed, layer thickness, and scanning strategy. These parameters have been demonstrated to have a direct influence on the solidification process, densification, and microstructure as well as properties of the fabricated MPEAs. Therefore, to fabricate MPEAs with desired microstructures and properties, it is essential to establish the processing-microstructure-property relationships for PBF of MPEAs. As such, great efforts in the past few years have been made to uncover the optimized PBF processing parameters for fabricating MPEAs [56–59]. Several process optimization criteria have also been developed based on different mechanisms, including the well-known volume energy density (VED) criterion:

$$\text{VED} = P/vth, \quad (1)$$

where P , v , t , h is the laser power, scanning speed, layer thickness and hatch space, respectively. It is worth noting that machine learning-based process optimization approaches have also been reported in recent years [60–62]. However, since different MPEAs have distinct physical and chemical characteristics and, thus, different responses to laser and electron beam, carefully designed experiments, physics-based computational modeling, and data-driving machine learning approaches should be combined and wisely integrated to obtain the optimized PBF process window for specific MPEAs [63].

Directed energy deposition (DED)

DED is another popular AM technology for processing MPEAs. Compared with the pre-laid metal powder in PBF, DED uses a heat source, which can be an electron beam, electric arc, or a laser beam, to simultaneously melt raw materials which are deposited in the form of powder or wire onto a substrate. The raw materials feed system, which may include several material sources (e.g., powder and wire), offers more options for processing MPEAs with different compositions. It can apply single nozzle with MPEAs powder/wire or multiple nozzles for

in situ mixing and melting different pure element powders/wires [64–66].

Compared with LPBF, DED has a lower cooling rate (10^3 – 10^5 K/s) and a lower manufacturing accuracy [36]. DED is the most popular method for the fabrication of MPEA coatings. Currently, it has successfully deposited 3d transition metal MPEA, Al added MPEA, and refractory MPEA coatings to give improved wear resistance, corrosion resistance, and/or strength [67–72]. Additionally, DED has some advantages for the fabrication of bulk MPEA components. These advantages derive from the powder/wire feed systems that enable changes in composition during the DED process across different layers which provides significant potential for fabricating functionally graded MPEA components with tailorable compositions, microstructures, and properties [73–77]. Without the manufacturing size limitation of the PBF, DED is reported to be able to fabricate large MPEA components (e.g., up to $5000 \times 3000 \times 1000 \text{ mm}^3$) with a high deposition rate (up to $300 \text{ cm}^3/\text{h}$) [36, 78].

Key advantages and main driving force for AM of MPEAs

High cooling and solidification rates

Compared with pure metals and traditional alloys, MPEAs are more likely to form intermetallic compounds and suffer from composition segregation due to the presence of multi-principal elements [79–81]. However, the ultrahigh high cooling rate of AM technologies, which ranges from 10^3 to 10^7 K/s, can significantly mitigate existing issues which reside in conventional manufacturing of MPEAs such as coarse grains and chemical segregation in large MPEA castings and forgings [45, 82, 83]. In detail, the high degree of undercooling induced by the high cooling rates used in AM can accelerate the movement of the solid–liquid interface during AM of MPEAs. In this process, the diffusion of elements in MPEAs is suppressed and trapped by solidification to form a solid solution. As the cooling rate increases, the microstructure changes from dendritic structures to chemically homogeneous cellular structures [77, 84, 85]. Furthermore, a high degree of undercooling and a fast moving solid–liquid interface can also increase the nucleation rate and restrain grain growth to form fine grain structures, or even

nanograins, leading to superior mechanical properties [86, 87].

Localized melting and solidification for microstructure tailoring in MPEAs

The ultrahigh energy sources (e.g., laser, electron beam, etc.) in AM can theoretically melt all the principal elements in MPEA powders or wires to form a melt pool which has been regarded as a unique characteristic and a meso-structure in AM fabricated metals and alloys [88, 89]. It has been shown that inside these melt pools, localized melting and solidification can enable the tailoring of the microstructure (e.g., grain size, precipitation, bimodal structure, etc.) of the fabricated metals and alloys by controlling the AM processing parameters and can also decrease the composition segregation in fabricated metal components [90–92]. Due to the relationship between the global and local heat flux during the AM process and grain growth, crystallographic texture of AM MPEAs can also be readily designed through controlling the power, hatch space, and scanning strategy to manipulate the solidification process within each melt pool.

Manufacturing of complex structures for various industrial applications

MPEAs are considered promising materials for various applications for aerospace, transportation, biomedical devices, etc. [6]. However, these emerging and complex materials are difficult to manufacture or process, which has imposed some restriction on the actual applications of MPEAs. A unique strength to AM technology is direct manufacturing with a computer-generated digital model, which eliminates the time-consuming and costly design and usage of mold/die design as well as multiple post-processing stages. The layer-by-layer fabrication in AM can lower the production requirements and offer new opportunities to efficiently integrate the design and manufacturing of complex-shaped MPEAs for various applications [93–95]. Therefore, in comparison with conventional MPEAs manufacturing techniques, AM technology has the potential to improve the accuracy and efficiency in both the design and production process while reducing waste of energy, materials, and human recourses. Reducing material waste is especially important for MPEAs since they

often have higher raw material cost than traditional alloys due to the large content of more expensive elements (e.g., Co and Ni) [96].

Real-time monitoring of the manufacturing process

It is quite challenging to observe the evolution of microstructure and solidification condition during most conventional manufacturing processes for MPEAs. However, AM is a layer-by-layer manufacturing process, which enable the in situ monitoring of each layer during the fabrication process. In situ monitoring systems such as high-speed cameras, IR cameras, or photodiode-based melt pool monitoring systems can be installed in the AM system to capture the key characteristics during the melting and solidification process of each layer and analyze the fraction and category of processing defects, which provides real-time feedback for adjusting the process to improve the robustness of the manufacturing process [97, 98]. As such, the continued development of real-time process monitoring methodologies is believed to underpin the future production of defect-free and robust MPEA components via AM.

Key microstructure features and characteristics in AM MPEAs

Densification and defects formation during AM

Since processing defects such as porosity, cracks, and element segregation are the main reasons for inferior mechanical properties of AM fabricated parts, determining how to optimize the AM process to fabricate high quality and fully dense parts with no or minimal processing defects is a high priority for AM research. However, up until now most MPEAs fabricated by AM still suffer from various processing defects [99–103]. In addition to MPEA powder feedstock, the AM processing parameters are considered as the main factors controlling the densification process of AM MPEAs. For instance, the relationship between the volume energy density (VED) and the relative density of LPBF FeCoNiCuAl was investigated and established by Ren et al. [104]. It was found that poor densification was generally caused by incomplete melting with low VED and keyhole formation with high VED, both leading to the formation of pores in the fabricated MPEA parts.

Kuzminova et al. [105] investigated CoCrNiFe MPEAs fabricated using a range of different VED, as shown in Fig. 1. The results showed that most porosity can be eliminated at a VED of 250 J/mm^3

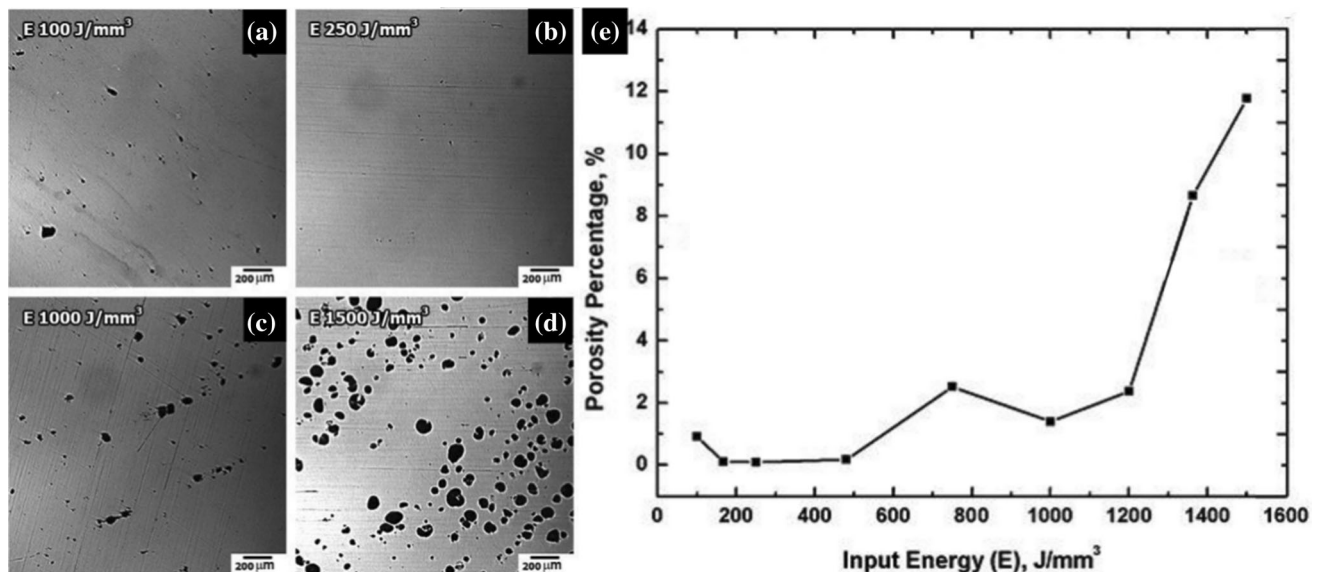


Figure 1 Optical microscopy images of CoCrNiFe MPEAs fabricated by LPBF using different VED: **a** 100 J/mm^3 , **b** 250 J/mm^3 , **c** 1000 J/mm^3 , **d** 1500 J/mm^3 . **e** The porosity percentage as

a function of input energy [105]. Reproduced with permission from Elsevier [ref. no. 5173901043280].

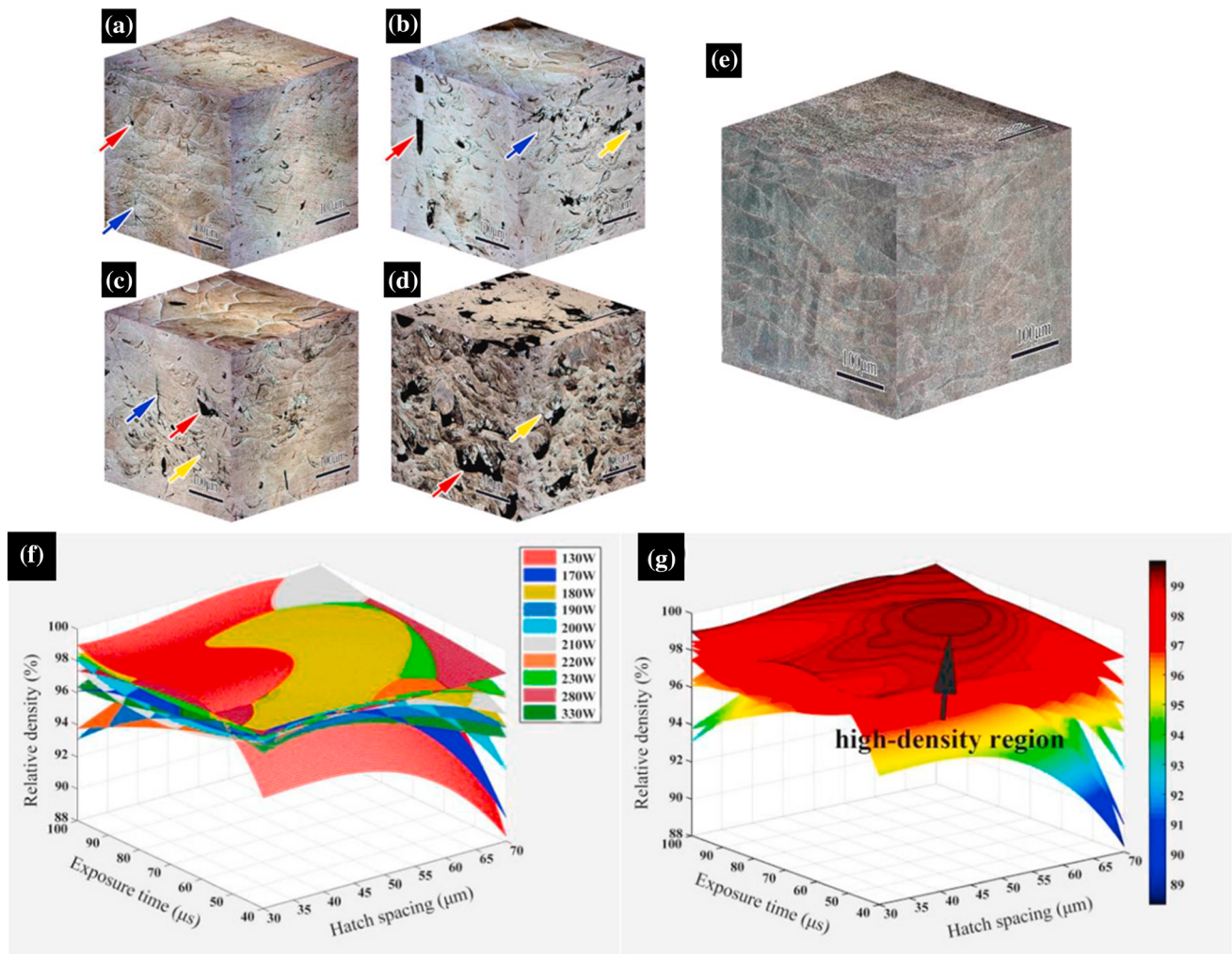


Figure 2 Optical microscopy images of samples with the same VED of $\sim 170 \text{ J/mm}^3$ but different power, hatch space and scanning speed: **a** 300 W, 110 μm and 400 mm/s; **b** 400 W, 150 μm and 390 mm/s; **c** 400 W, 200 μm and 295 mm/s; **d** 50 W, 20 μm and 368 mm/s; and **e** 203.6 W, 41.6 μm and 74 mm/s, respectively. Blue arrows show cracks, red arrows show porosity,

and yellow arrows show un-melted particles. Effects of parameter combinations on the relative density of the LPBF fabricated CoCrNiFe MPEAs shaded according to: **f** laser power and **g** relative density [109]. Reproduced with permission from Elsevier [ref. no. 5173910645320].

while the porosity can reach 11.8% using a high VED of 1150 J/mm^3 . Similarly, Niu et al. [106, 107] fabricated AlCoCrNiFe and CoCrNi MPEAs by LPBF and investigated their densification process during LPBF. It was shown that the highest relative density of AlCoCrNiFe and CoCrNi can reach 98.4% and 98.9% at a VED of 97.2 and 83.3 J/mm^3 , respectively. As for CoCrNiFeMn MPEAs, Jie et al. [108] fabricated a series of MPEA samples with more than 99.5% relative density at a VED in the range 62.5–115.6 J/mm^3 . It can be concluded that the optimized AM processing parameters for MPEAs with different alloy compositions vary greatly, even when there is only a

minor difference in one element. Thus, careful work needs to be carried out for each individual MPEA to obtain its own and unique optimized AM processing window.

Even though VED to some extent can be an effective criterion for optimizing the LPBF process, due to the complexity of LPBF, other influential processing parameters should also be considered, e.g., the diameter of the laser beam and the scanning strategy. Lin et al. [109] fabricated CoCrNiFe MPEAs using different combinations of LPBF parameters with the same VED of 170 J/mm^3 (Fig. 2a–d). The results showed very different microstructures as well as

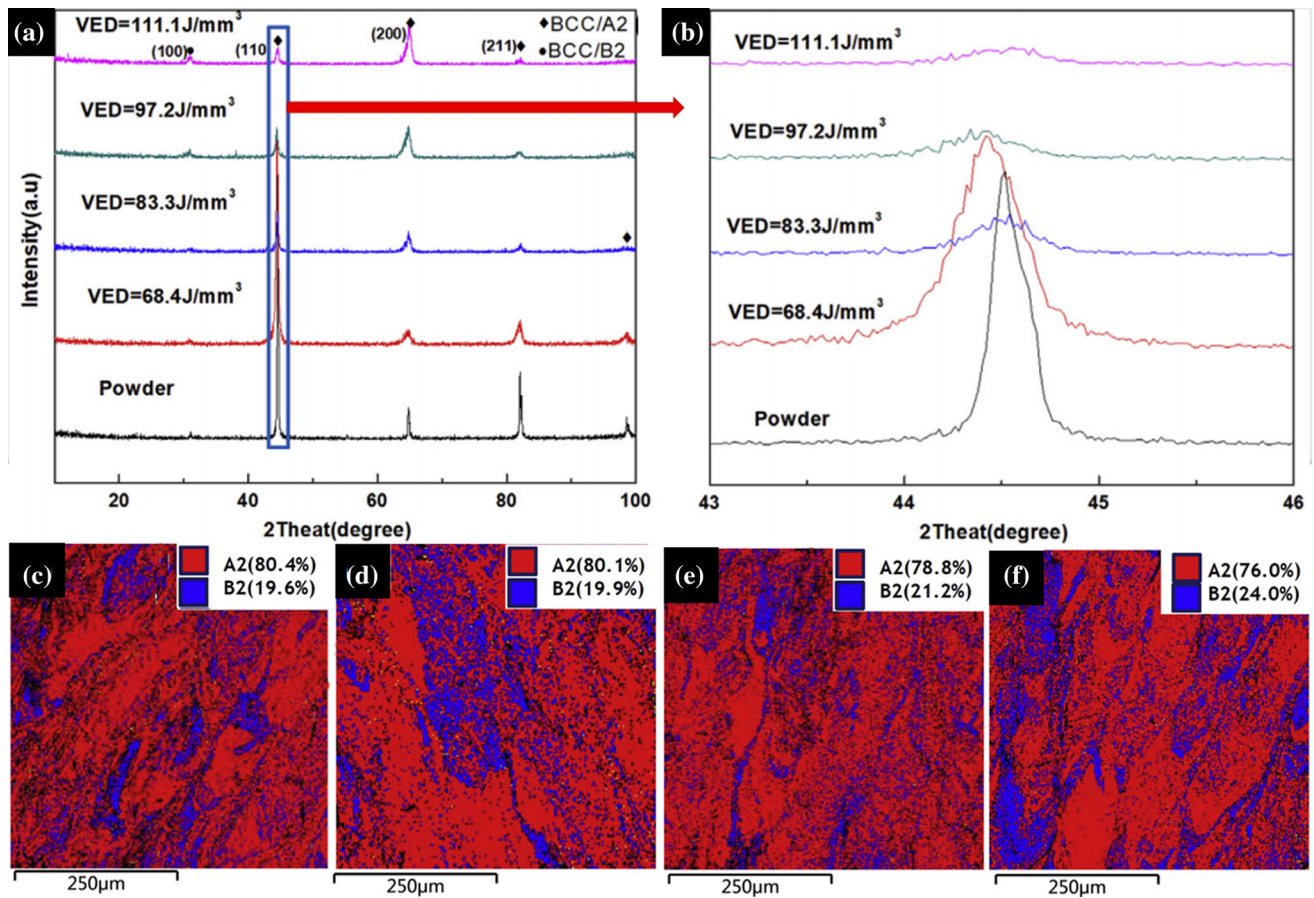


Figure 3 XRD patterns of the AlCoCrFeNi powder and LPBF fabricated AlCoCrFeNi samples: **a** the influence of different VED; **b** enlarged image of the (110) peaks from (a). The phase distribution in different AlCoCrFeNi samples fabricated by LPBF

at different VED: **c** 68.4 J/mm³; **d** 83.3 J/mm³; **e** 97.2 J/mm³; **f** 111.1 J/mm³ [107]. Reproduced with permission from Elsevier [ref. no. 5173910874611].

porosity level and confirmed that the densification is not simply correlated to VED. At the same time, they proposed a multiple regression model (Fig. 2f, g) based on polynomial regression analysis to accurately illustrate how the densification varies with multiple parameter combinations and validated its practicability by successfully fabricating a fully dense MPEAs part with a relative density of 99.71% (Fig. 2e). In addition, Zhou et al. [110] presented a model to predict the proper LPBF parameters for fabricating high quality MPEAs parts. The model uses the physical characteristics of the materials such as laser absorptivity, latent heat of melting, and specific heat capacity to calculate energy absorption (Q_a) and energy consumption (Q_c), and it predicts that an ideal part can be built when Q_a/Q_c has a value between 3 and 8. Based on this model, they successfully fabricated a CoCrNiFeMn sample with 99.9% relative density.

Cracks are another common processing defect in AM MPEAs [106]. While porosity in PBF is mainly caused by incomplete or excessive melting process, cracks are believed to be generally caused by thermal stresses and element segregation. For instance, Sun et al. [100] investigated the mechanisms for hot tearing in CoCrNiFe fabricated by various LPBF process parameters and scanning strategies. Intergranular hot cracks were found in all the samples with no element segregation, revealing that residual stresses caused by the coarse grain size were the major reason for hot crack formation.

MPEAs fabricated by DED technology are more commonly used in coating applications; thus, there are few studies reported on the actual densification process while most of previous studies are focused on the formation of processing defects during DED [86, 111, 112]. For example, Henrik et al. [113] fabricated TiZrNbTa MPEAs by DED and found that the

proper feeding speed of nozzle (100 mm/min) can lead to high quality MPEAs samples. Moreover, Modupeola et al. [114] investigated the influence of processing parameters on the microstructure of DED fabricated AlTiCrFeCoNi and AlCoCrFeNiCu MPEAs. They indicate that using a laser power of 1200–1600 W and a scanning speed of 8–12 mm/s can result in reduced processing defects than other parameters. Meanwhile, they also applied a pre-heating strategy with a temperature of 400 °C and demonstrated its effect on the reduction of cracks through eliminating residual stresses during the DED process.

Phase formation and evolution in AM MPEAs

In general, the phase composition of AM produced MPEAs correspond well to the composition of the same MPEAs produced by conventional manufacturing processes, e.g., casting. For instance, Brif et al. [49] investigated the FeCoCrNi MPEA fabricated by LPBF and found that only FCC solid solution was produced, which is consistent with the phase formation in the previously reported FeCoCrNi MPEAs fabricated by induction and arc melting [115–118].

However, for Al containing MPEAs, phase transitions have been found to be strongly related to the AM processes [51]. Prealloyed AlCoCrFeNi powder with A_2 (disordered BCC phase) + B_2 (ordered BCC phase) structures was used for LPBF processing by Niu et al. [107]. It was found that the as-built AlCoCrFeNi kept the A_2 + B_2 phase structure, and the B_2 phase was first formed at the boundary of the melt pools where a higher cooling rate existed. From the XRD profiles and phase composition maps shown in Fig. 3, the amount of A_2 phase decreased and the amount of B_2 phase increased with increasing VED [82, 119]. Additionally, composition variation also affects the phase formation and evolution in AM MPEAs. For instance, Sun et al. [120] produced Al_x-CoCrFeNi with LPBF and found a FCC to BCC/ B_2 + FCC and then to BCC/ B_2 transition with increasing Al content from 0 to 1%, and all BCC/ B_2 phases are emerging and located in the interdendritic and grain boundaries area. Li et al. [121] also reported a phase formation in DED fabricated (CrMnFeCoNi)_{1-x}Fe_x, a BCC phase emerged when added 60% Fe into equal atomic ratio CrMnFeCoNi MPEAs. More interestingly, a phase transition from BCC to

FCC was found in LPBF AlCrCuFeNi_x by Luo et al. [53]. It is reported that microstructure consisted of a B_2 phase matrix and disordered BCC phase in AlCrCuFeNi_{1.0} (Fig. 4a, b). Increasing the Ni ratio from 1.0 to 3.5 caused a lamellar FCC phase to form, while the relative fraction of basket weave and B_2 matrix decreased and transformed into a spherical morphology (Fig. 4c, d).

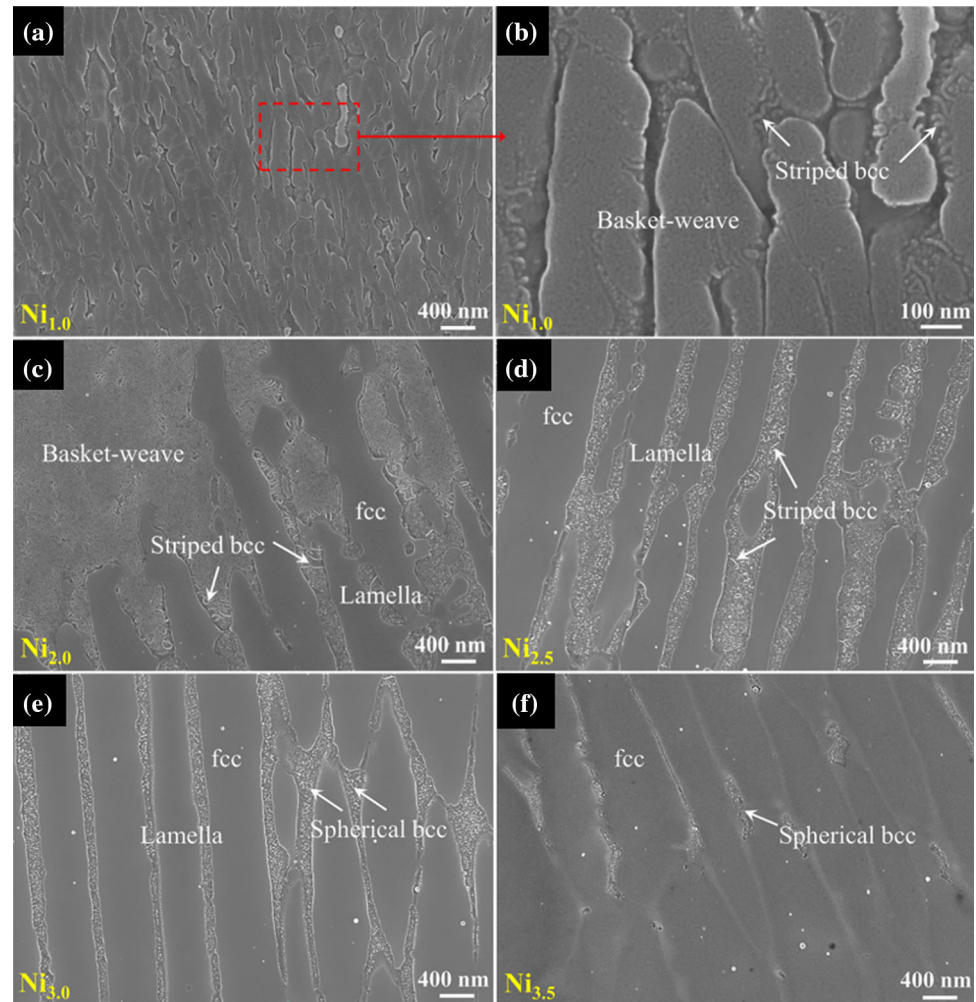
Solidification microstructure of AM MPEAs

It is known that the layout and morphology of the melt pool can affect the solidification microstructure in the AM MPEAs. Piglione et al. [122] carried out a detailed study of the solidification microstructure in LPBF fabricated CoCrNiFeMn MPEAs in both single layer and bulk samples. Solidification in the single layer occurred via the growth of grains and a fine cellular structure along the direction of maximum heat flux, i.e., from the existing grains in the substrate toward the center of the single layer top surface (Fig. 5a–c). For the bulk sample, however, columnar grains formed primarily from the substrate and developed via growth competition among different directions (Fig. 5d–f). It was concluded that highly directional heat flux promoted columnar growth of the solidifying grains that followed the thermal gradient and restrained other growth directions by multiple remelting processes.

AM processing parameters impact not only the processing defects but also the solidification microstructure [114, 123]. Tong et al. [124] uncovered the influence of DED processing parameters on the solidification of CoCrNiFeMn MPEAs. The microstructural feature in the vertical section is dendritic columnar grains which become coarser with increasing laser power (Fig. 6a–c). Since the dendritic columnar grains grow parallel with the build direction, the horizontal section of the columnar grains showed an equiaxed morphology with the dimensions increasing with higher laser power (Fig. 6d–f).

The influence of processing parameters on the microstructure of LPBF fabricated CoCrFeNiTi was reported by Takafumi et al. [93], with a focus on the morphology of a single track scan. The results showed that lower laser power, higher scanning speed and smaller laser spot diameter would cause a discontinuous melt track. Moreover, a surface texture parameter (S_a) was introduced to evaluate the correlation between the crystallographic texture and the

Figure 4 HRSEM images showing the microstructure evolution for the LPBF AlCrCuFeNi_x MPEAs: **a** Ni_{1.0}; **b** high magnification of red box area of **a**; **c** Ni_{2.0}; **d** Ni_{2.5}; **e** Ni_{3.0}; **f** Ni_{3.5} [53]. Reproduced with permission from Elsevier [ref. no. 5187670568261].



LPBF processing parameters. The S_a value decreased with increased scanning speed and power and the surface roughness was improved for a given VED value, as shown in Fig. 7a. It was also shown that the solidification microstructure was largely dependent on the VED. As VED increased from 20.8 to 83.3 and then to 333 J/mm³, the depth and width of the melt pool trace observed from both planes showed a conspicuous difference (Fig. 7b–g). Regarding the grain morphology, higher VED allowed laser energy to transfer through more layers to promote the growth of columnar grains (Fig. 7h–j).

Cellular microstructures are a common feature in AM MPEAs, and they result from high-density dislocation tangling and/or element segregation during the rapid solidification process [51, 125, 126]. Yang et al. [127] reported a cellular microstructure in LPBF fabricated CrFeNiMn MPEAs. Equiaxed and elongated cells can be seen inside the grains in Fig. 8a, b.

Moreover, an ultra-fine sub-cell structure formed inside the cells (Fig. 8c). The TEM results showed that high-density dislocations were concentrated on the cell walls, as shown in Fig. 8d. The formation of the ultra-fine sub-cells was mainly due to the dislocation tangling inside the cells, which is seen in Fig. 8f. EDS results in Fig. 8e–g revealed the segregation of Mn and Ni in the concentrated dislocations areas, as well as in the dendritic, cell boundaries and even sub-cell boundaries. The formation of cellular microstructure occurs in this case when elements with lower melting point (e.g., Mn and Ni) enrich in the solid–liquid interface which has a slower solidification rate than regions enriched with high melting point elements (e.g., Cr and Fe).

Anisotropic microstructures in AM MPEAs generally arise from the combined effects of directional global and local heat flux, build orientation, and scanning strategy [128–130]. The microstructure of an

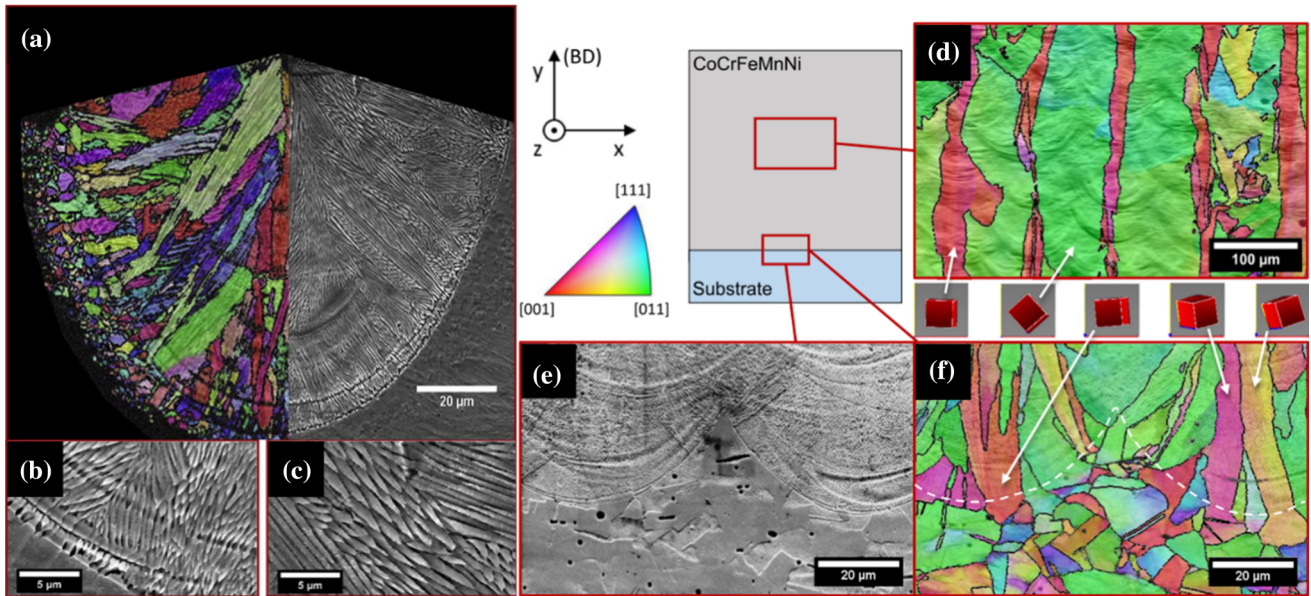


Figure 5 a SEM image and related EBSD IPF map showing the morphology of the cross section of single track of LPBF fabricated CoCrNiFeMn MPEAs. b and c SEM images showing the morphology of the cellular structure in (a). d EBSD IPF map of

a region in the LPBF fabricated CoCrNiFeMn cube. e and f SEM images and related EBSD IPF map showing the morphology of the substrate/build interface in the samples [122]. Reproduced with permission from Elsevier.

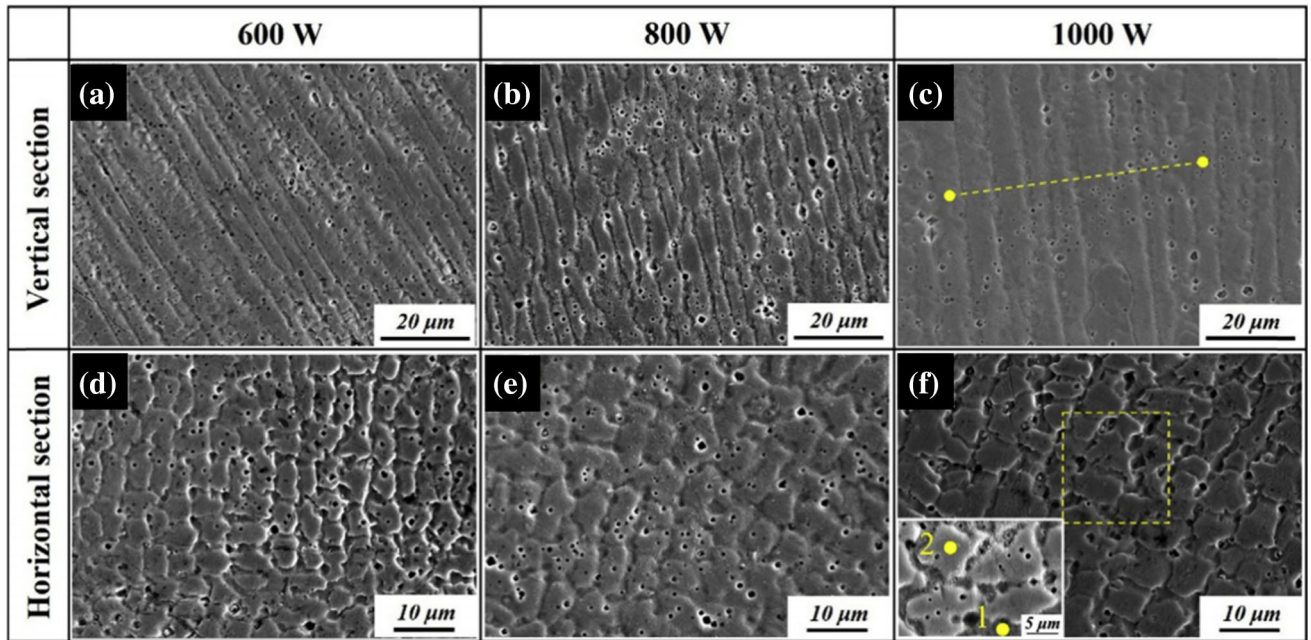


Figure 6 SEM images showing the morphology of the vertical and horizontal sections of DED processed CoCrNiFeMn using different laser powers: a and d 600 W, b and e 800 W, c and

f 1000 W [124]. Reproduced with permission from Elsevier [ref. no. 5173920449665].

LPBF fabricated part can be approximated as a continuous overlay of single melt pools. As such, an unsymmetrical melt pool can cause different solidification behavior/processes along different

directions. For example, Jeong et al. [131] reported an LPBF produced (CoCrFeMnNi)₉₉C₁ MPEA. It has an anisotropic solidification microstructure in YZ, XZ, and XY planes caused by applying a bi-directional

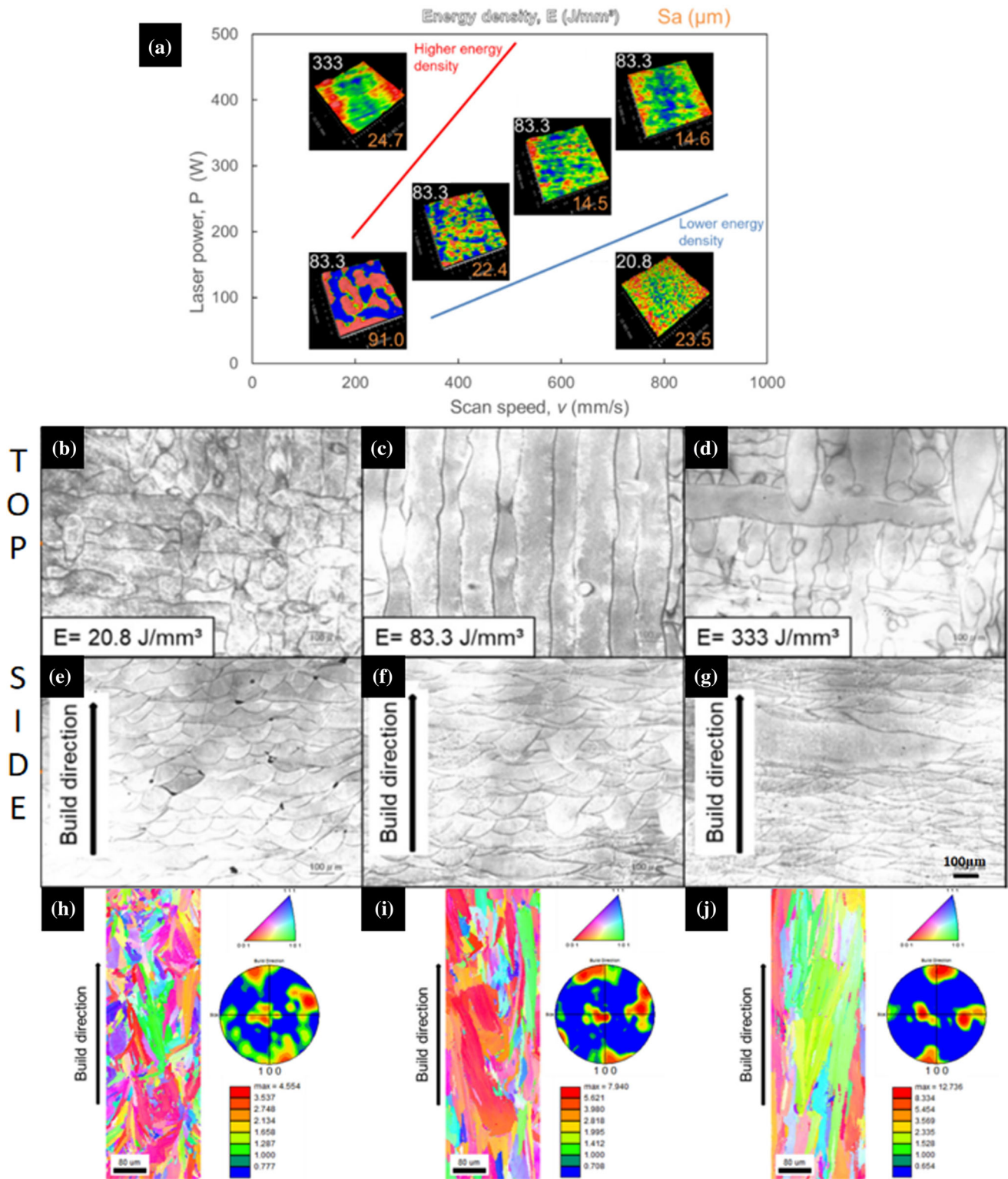


Fig. 7 a Surface texture parameter (S_a)-based LPBF processing map with respect to laser power and scan speed; Optical microscopy images of the top surface, side surface and IPF map with pole figures for LPBF CoCrFeNiTi fabricated using different

energy density: **b**, **e** and **h** 20.8 J/mm³, **c**, **f** and **i** 83.3 J/mm³, **d**, **g** and **j** 333 J/mm³, respectively [93]. Reproduced with permission from MDPI.

scanning strategy (Fig. 9a–c). Also, grains of the LPBF produced $(\text{CoCrFeMnNi})_{99}\text{C}_1$ show anisotropic growth because of heat flux distribution in the melt pool (Fig. 9d, e).

Heat flux was demonstrated to play a key role in determining the growth direction of both grains and internal cells in a single melt pool [84, 92, 114]. It is known that by changing the scanning direction a different heat flux with different directions can be obtained in the melt pool of the fabricated part. Following this, the apparent anisotropy in both crystallographic texture and grain morphology as a function of different scanning strategies was extensively investigated in the past few years. For example, Bogdan et al. [132] assessed the microstructure of LPBF fabricated CoNiCrFeMn with various scanning strategies. One conclusion which was drawn from the study was that applying a scanning strategy with 67° rotation can contribute to higher relative density (about 99.7%) than that with 0° and 90° (about 99.2%). It was also demonstrated that the grain morphology and crystallographic texture were highly consistent with meander and chessboard scanning strategies, especially for the equiaxed grain aligned in the Z direction (Fig. 10a–d). A sample with 67° rotation between two consecutive layers using a chessboard strategy (Fig. 10e, f) produced a spiral grain structure

(Fig. 10g, h), which further confirmed that the scan strategies could be used to design and control the crystallographic texture and morphology of the solidification grain structure.

Additionally, the chemical composition and distribution dramatically impact the solidification microstructure of AM MPEAs [53]. With the advantage of DED in producing compositional graded MPEAs, Borkar et al. [133] reported the microstructure of $\text{Al}_x\text{CrCuFeNi}_2$ by DED, as shown in Fig. 11. A typical dendritic microstructure was observed in the Al-free MPEA and particles distributed on the cellular boundaries were confirmed to be Cu segregation. A needle-like secondary phase structure with dark contrast was revealed in DED fabricated $\text{Al}_x\text{CrCuFeNi}_2$ with $x = 0.8$. Upon increasing the Al content, fine equiaxed grains with intragranular BCC/ B_2 phase and intergranular FCC phase were formed and the relative amount of BCC/ B_2 phase continued to increase until $x = 1.5$.

Some progress has been made in AM processing of refractory MPEAs [43, 68, 134] in the past five years. For instance, Takuya et al. [85] developed a structural TiNbTaZrMo BioHEA by LPBF (Fig. 12a) and validated its suitability for biomedical applications. A BCC solid solution structure was generated and found to have an anisotropic grain distribution

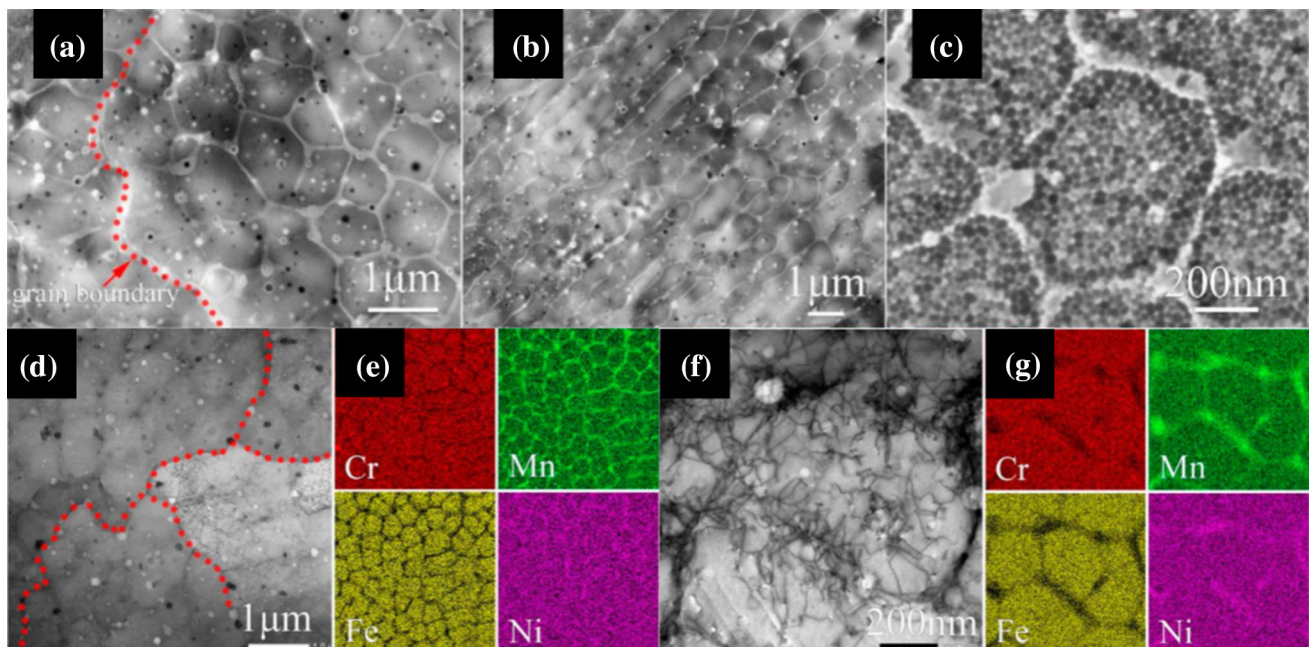


Figure 8 SEM images of LPBF fabricated CrFeNiMn microstructures: **a** equiaxed cells; **b** elongated cells, and **c** ultra-fine sub-cells. TEM images of LPBF CrFeNiMn microstructure:

d equiaxed cells and **f** magnified equiaxed cells with their corresponding EDS maps of elements distribution, **e** and **g** [127]. Reproduced with permission from MDPI.

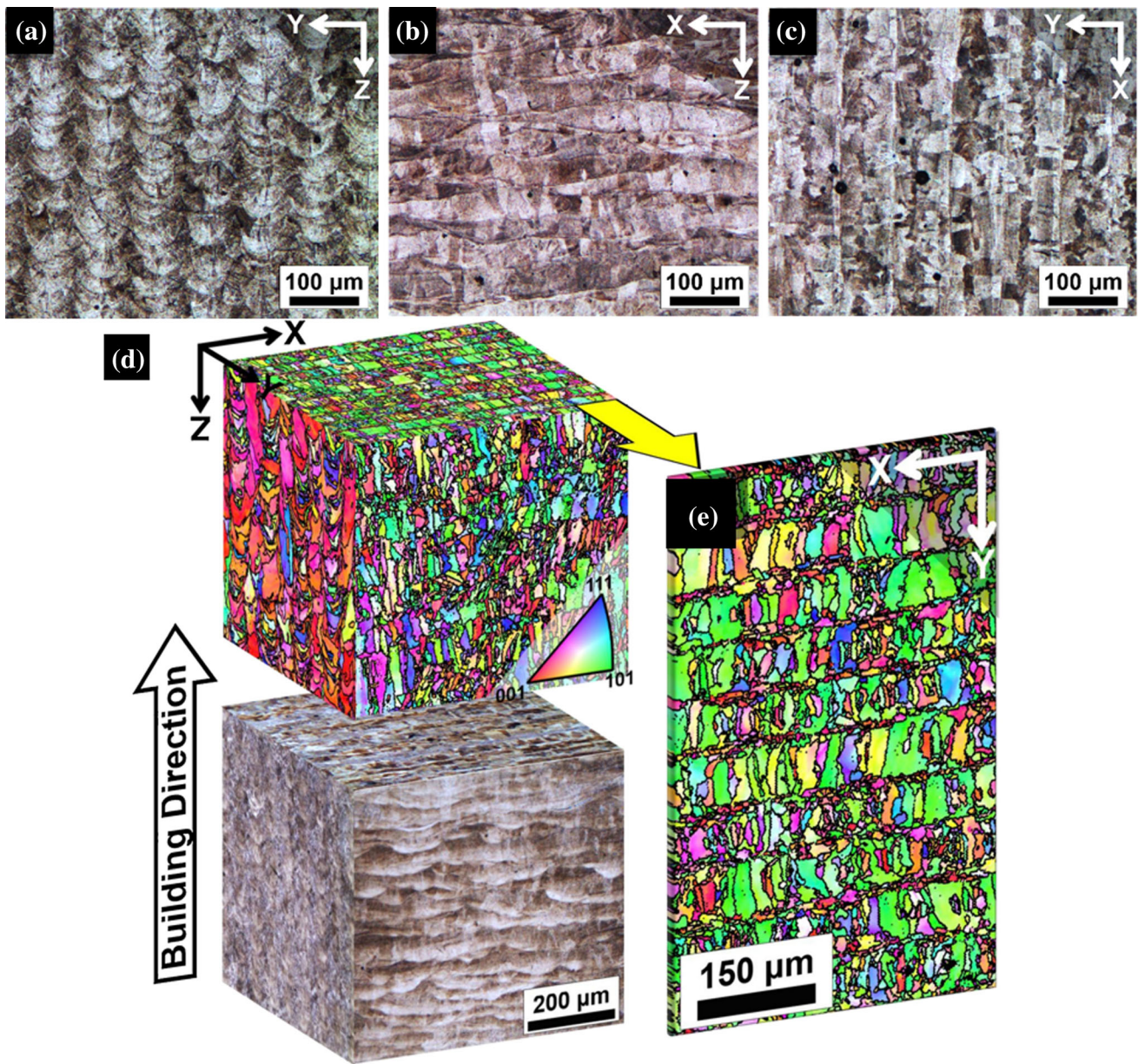


Figure 9 Optical microscopy images for the etched surfaces of the LPBF processed $(\text{CoCrFeMnNi})_{99}\text{C}_1$ with respect to **a** X; **b** Y; and **c** Z planes. 3D visualization of LPBF processed HEA: **d** IPF maps

(top) and OM images (bottom) for three orthogonal planes, and **e** magnified view of IPF map from Z plane [131]. Reproduced with permission from Elsevier [ref. no. 5173920213421].

corresponding to the melt pool tracks. Fine grains clustered along the boundary of the melt track while coarse grains centralized in the melt track on the XY plane (Fig. 12c). It was also shown that in the YZ plane, columnar grains along the cross section of the melt pool were caused by a 90° rotation scanning strategy (Fig. 12d). Fine equiaxed grains were formed at the bottom of melt pool and columnar grains grew toward the melt pool center (Fig. 12e–g). Compared

with a conventionally cast sample, the elemental distribution in LPBF fabricated samples was relatively homogeneous, which was mainly attributed to the fact that a high cooling rate during AM can facilitate the formation of a solid solution structure with reduced element segregation (Fig. 12h–k).

Microstructural heterogeneity along the build direction in AM MPEAs

During AM of MPEAs, high heating and cooling rates as well as cyclic thermal profiles (i.e., cyclic heating and cooling) can generate microstructures that are very distinct from those obtained via traditional

Figure 11 a–f SEM images of DED AlxCrCuFeNi₂ with increasing Al content; g–l corresponding SEM images at higher magnification, White circles show secondary phase, yellow arrow shows along the grain boundary, red circle shows fine-scale FCC precipitates and white arrows show cellular/dendritic boundaries [133]. Reproduced with permission from Elsevier [ref. no. 5173961154619].

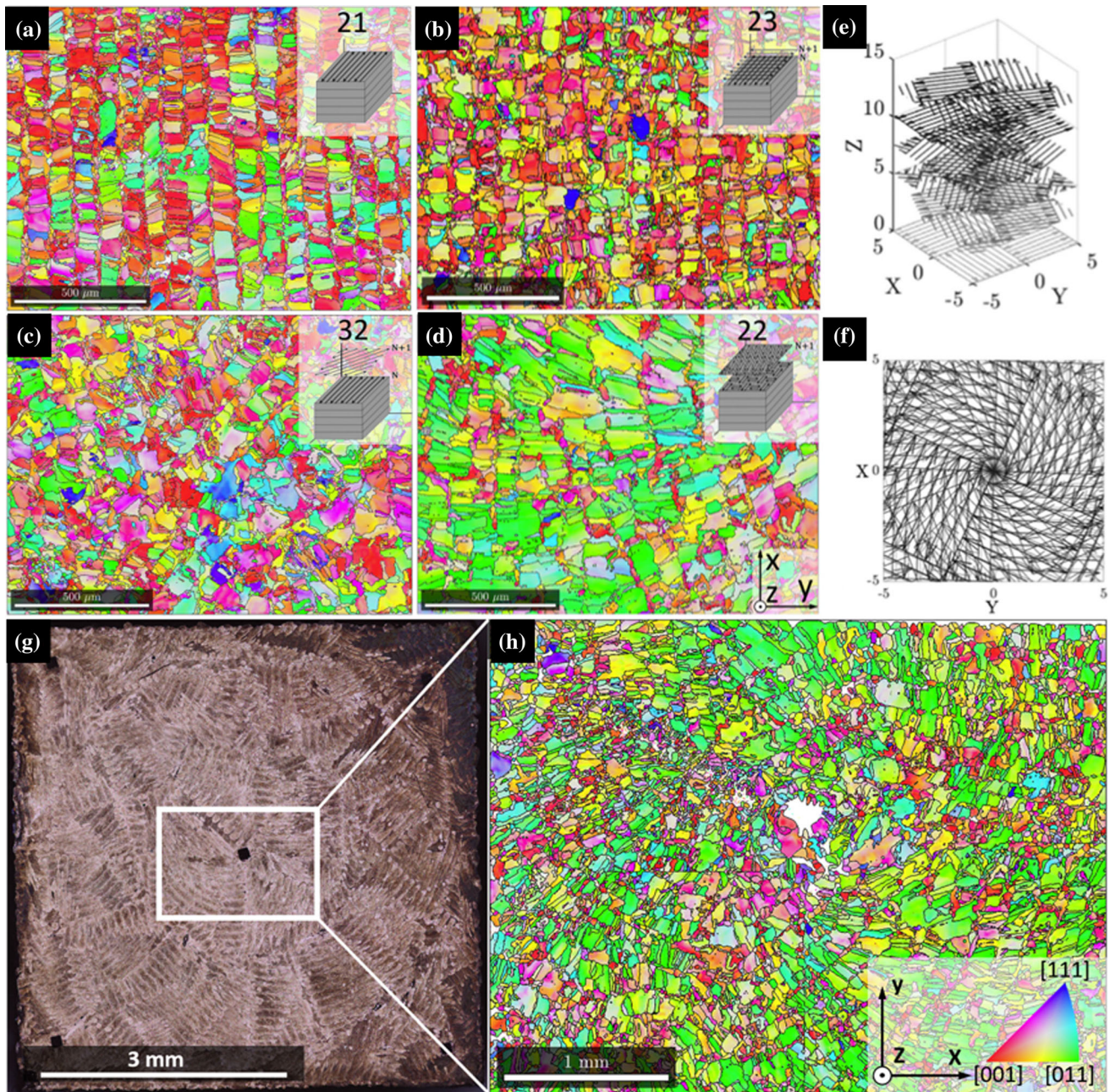
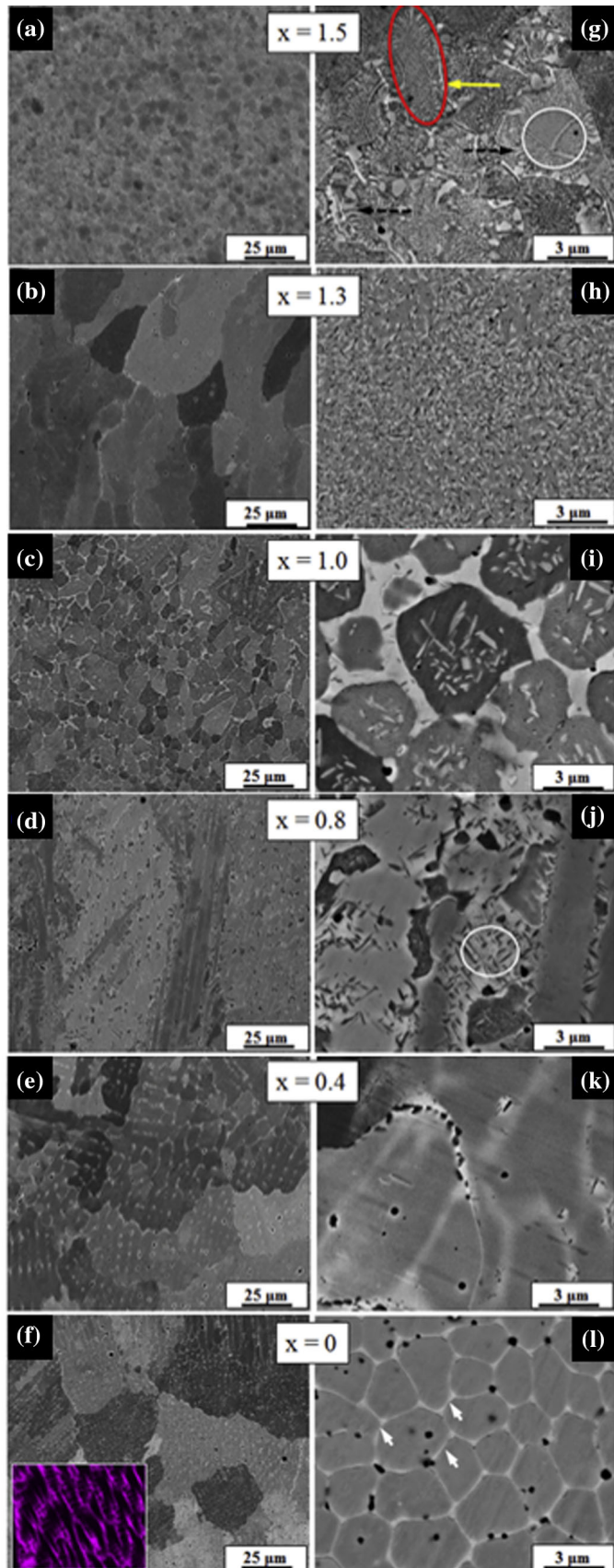
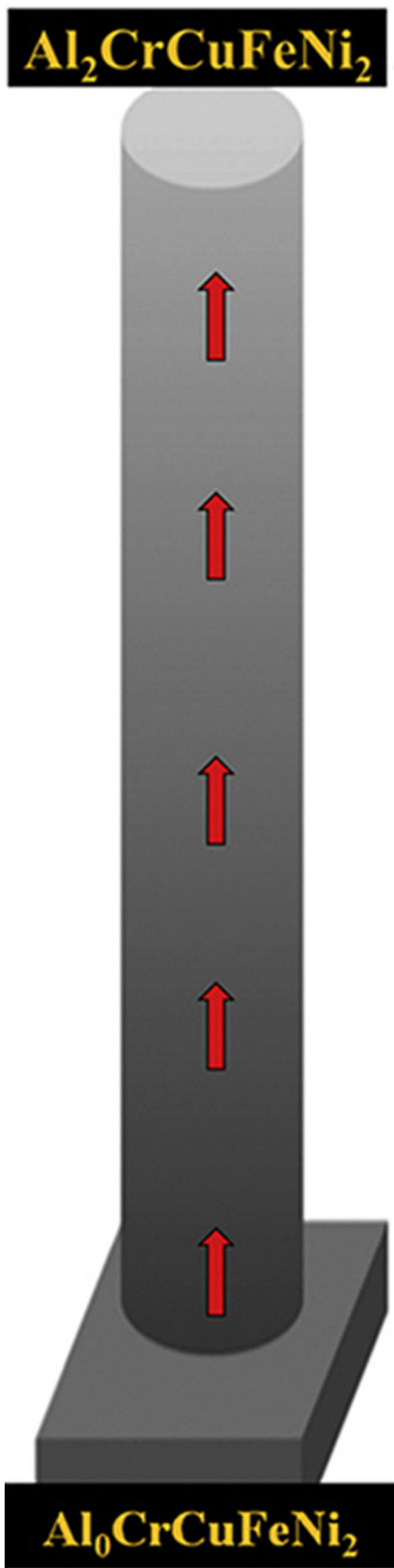


Figure 10 EBSD IPF maps from the top view of LPBF fabricated CoNiCrFeMn with **a** meander with 0° rotation, **b** meander with 90° rotation, **c** meander with 67° rotation, **d** chessboard with 67° rotation. **e** scanning directions across six consecutive layers for the

chessboard with 67° rotation, **f** corresponding top view, **g** OM images of LPBF CoNiCrFeMn fabricated by **e**. **h** EBSD IPF maps of the white square area of **g** [132]. Reproduced with permission from Elsevier [ref. no. 5173921058780].



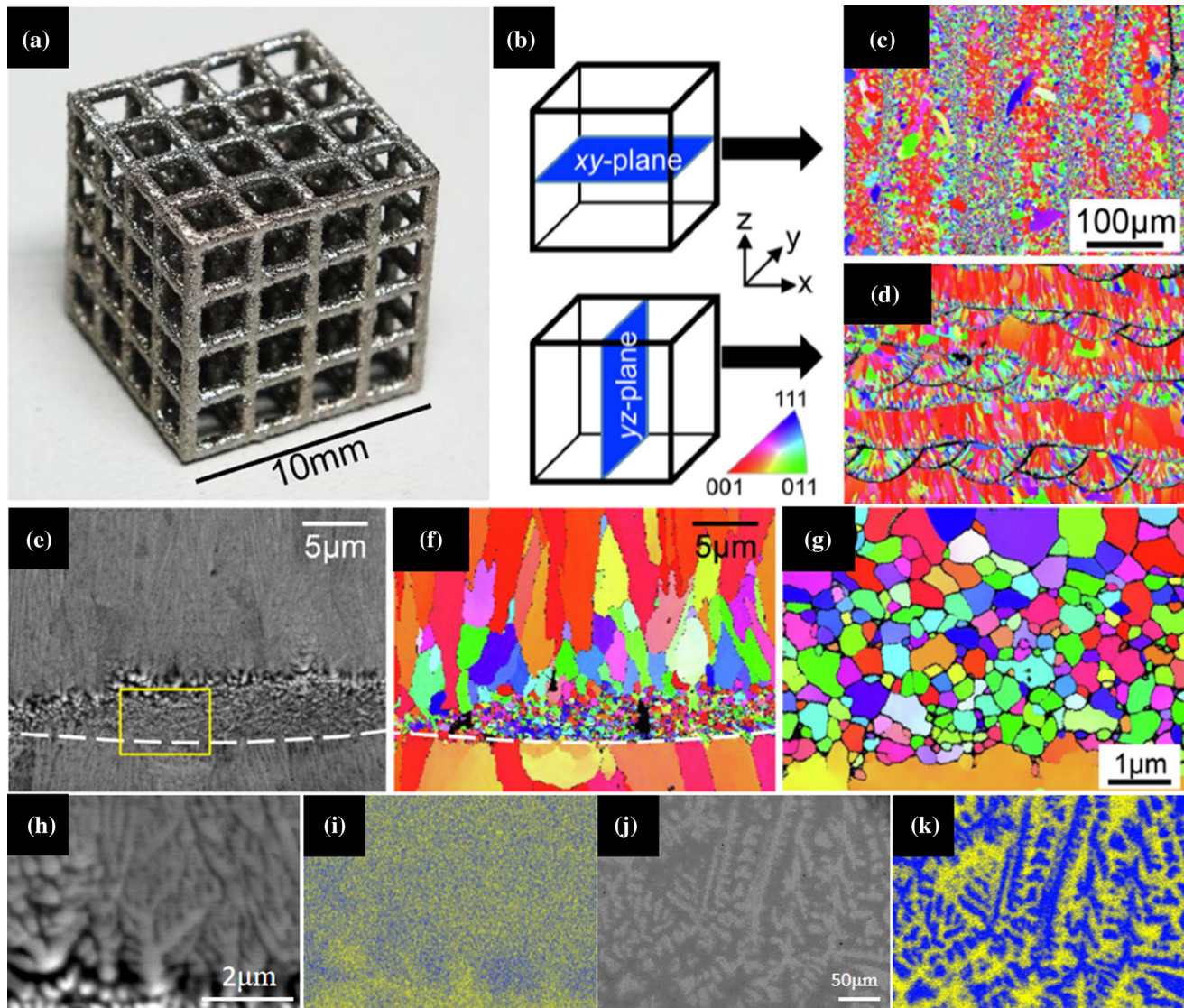


Figure 12 a LPBF fabricated lattice structure for a TiNbTaZrMo alloy. b EBSD IPF maps of c XY plane and d YZ plane. e SEM image of the bottom of melting pool. f corresponding IPF mapping and g IPF mapping at higher magnification. Dendritic structure and

corresponding EDS mapping in h and i LPBF fabricated TiNbTaZrMo, j and k casting TiNbTaZrMo [85]. Reproduced with permission from Elsevier.

manufacturing processes, in particular the heterogeneous and meta-stable microstructure in AM MPEAs. Unfortunately, the cyclic thermal profiles along with high heating and cooling rates during AM are quite complex phenomena to understand experimentally. This is mainly because in situ microstructural observation during AM is still quite challenging although more and more advanced in situ monitoring systems and techniques for AM have been developed recently. In recent years, great efforts have been made to uncover these above-mentioned unclear phenomena and some studies about the heterogeneity of

microstructures of MPEAs produced by AM were recently reported [125, 128, 135]. For example, Wang et al. [136] investigated the microstructural evolution of LPBF fabricated CoCrFeMnNi with respect to cyclic and rapid thermal profiles. In their study, five specimens from the built part along the building direction (Fig. 13a) were selected. It was found that nanograins with average size ranging from several nanometers to tens of nanometers (i.e., 50 to 70 nm) were observed in the top region I and II, respectively (Fig. 13b–e). In region III, grains of several micrometers in size containing a random distribution of

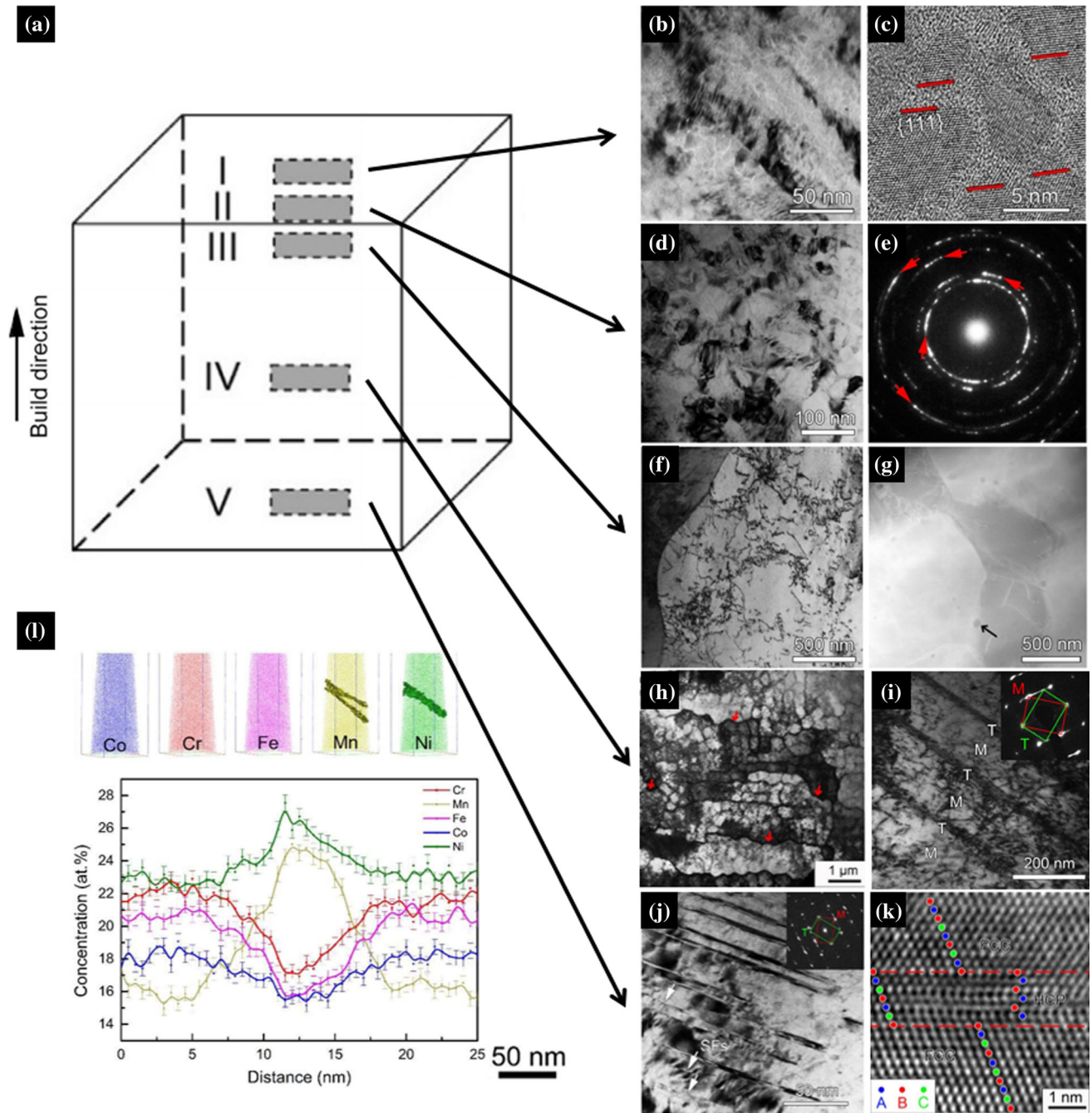
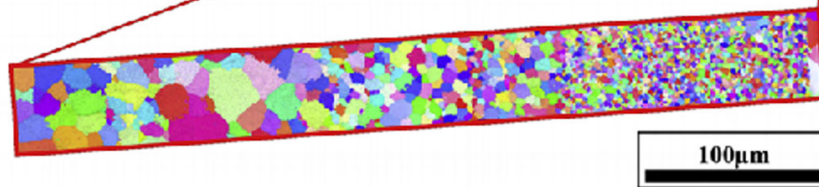
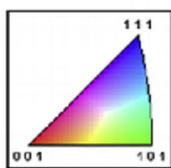
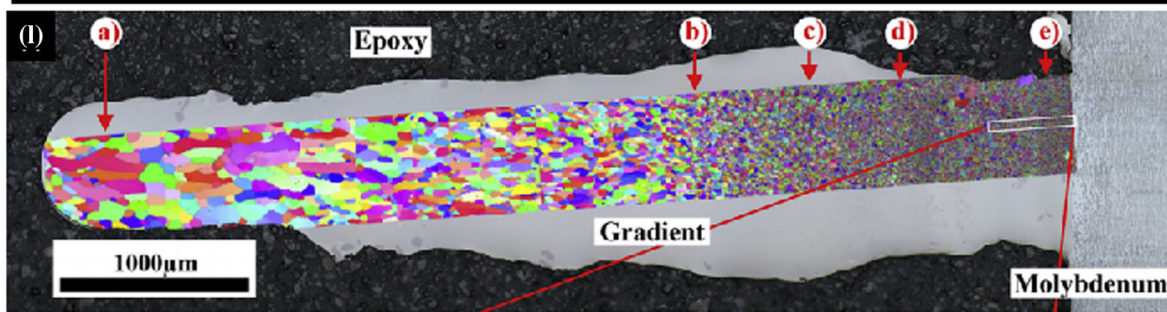
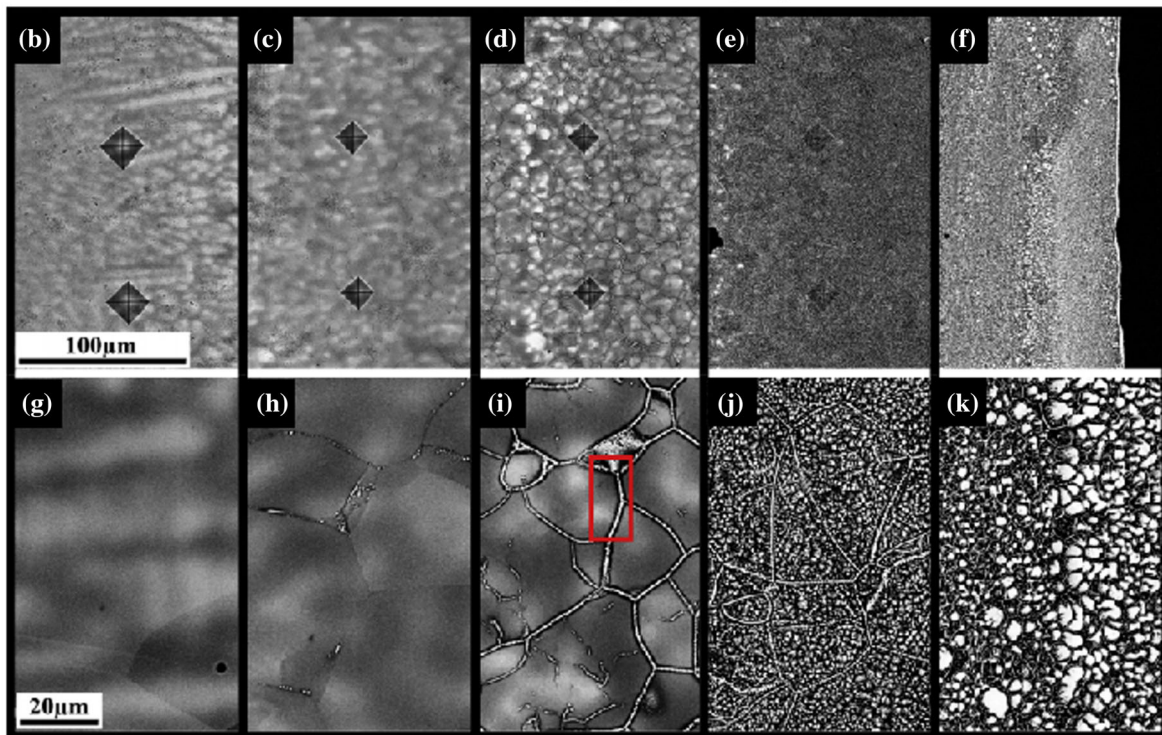
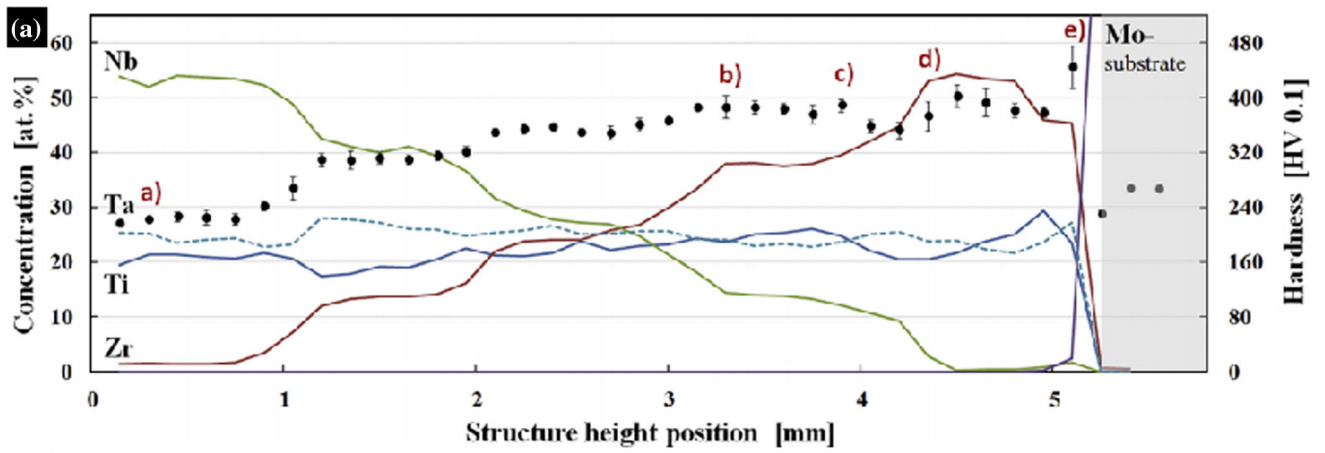


Figure 13 a A schematic illustration of a SLM fabricated CrMnFeCoNi alloy with marked region I to V. b–k TEM images corresponding to region I, II, III, IV and V, respectively [136]. l APT results from a middle layer of the SLM fabricated CrMnFeCoNi [137]. a–e Reproduced with permission from

Elsevier [ref. no. 5173970202568]. f–k Reproduced with permission from Elsevier [ref. no. 5173970350427]. l Reproduced with permission from Cambridge University Press [ref. no. 5173970646629].

dislocations were observed (Fig. 13f, g). The microstructure in region IV contained elongated grains of ~ 3.4 μm in length and 1.3 μm in width. Cellular substructures with high dislocation density were also observed within the grains in region IV

(Fig. 13h). Fine twins with 30 nm thickness were also observed to contain a random distribution of dislocations rather than a cellular substructure (Fig. 13i). In region V, there was an increase in the quantity of stacking faults and thinner nano-twinned structures



◀ **Figure 14** a Composition gradient ranging from $Ti_{23}Zr_{43}Nb_0Ta_{34}$ to $Ti_{23}Zr_0Nb_{42}Ta_{35}$ in a DED fabricated part and corresponding hardness value. b–f SEM BSE images showing the microstructure corresponding to locations a to e, (g–k are enlarged images of these locations). l SEM BSE image of the entire sample with overlaid EBSD IPF map, including a magnified IPF map of the sample in the vicinity of the Mo substrate/sample interface [113]. Reproduced with permission from Elsevier [ref. no. 5173970829239].

while the cellular dislocation substructure in these regions decreased (Fig. 13j). Moreover, an HCP phase was observed in Fig. 13k, revealing that an FCC to HCP phase transition occurred at the bottom of the sample. The atom probe tomography (APT) data, as shown in Fig. 13l, exemplified the segregation of Mn and Ni in dislocation cell walls, which can be elucidated by precipitation order and extent of partitioning of elements during solidification [137].

In addition to the LPBF fabricated MPEAs, both Cai et al. [64, 138] and Shou et al. [64, 138] fabricated an FeCoCrNi part using DED, which exhibited a heterogeneous microstructure consisting of a solidification grain structure with columnar grains at the bottom and equiaxed grains at the top of the fabricated MPEAs, respectively. Moreover, the composition gradient generated by the DED process can also lead to a heterogeneous microstructure. Henrik et al. [113] fabricated refractory MPEAs by DED with a composition varying from $Ti_{23}Zr_0Nb_{42}Ta_{35}$ to $Ti_{23}Zr_{43}Nb_0Ta_{34}$ (Fig. 14a). This composition change was accompanied by a change in microstructure from dendrites to fine grains in the matrix (Fig. 14b–k), with EBSD mapping revealing a decrease in average grain size from 60 to $\sim 2 \mu m$ (Fig. 14l). Overall, the heterogeneous microstructures exhibited by many MPEAs suggest that process parameter adjustment would be required during the build to achieve a homogeneous microstructure. Or, alternatively, there is a great opportunity to fabricate graded structures with location specific mechanical properties, for example harder at the surface and tougher at the subsurface.

Mechanical behavior of AM MPEAs

Mechanical properties are important selection criteria when considering AM MPEAs for various industrial applications. Compared with MPEAs fabricated through conventionally manufacturing techniques, MPEAs produced by AM generally exhibit superior hardness, strength, and fatigue resistance [111, 121, 130]. This enhancement in mechanical properties is mainly attributed to solid solution strengthening, grain boundary strengthening, and dislocation strengthening, which are closely related to the high heating and cooling rates as well as layer-wise manufacturing nature endowed by AM [139]. Comprehensive understanding of mechanical behavior of AM MPEAs can underpin the design and manufacturing of MPEAs with desired properties for potential applications.

Hardness of AM FCC MPEAs such as CoCrFeNi, CoCrFeNiMn, and $Al_{0.5}CoCrFeNi$ vary from 200 to 400 HV [92, 105, 140]. Introducing BCC phases or secondary particles by adding Al, C, B and Ti can generally increase the hardness in AM MPEAs (Fig. 15a) [107, 133, 141]. Refractory MPEAs, either fabricated using AM or conventional manufacturing methods, often exhibit higher hardness due to their BCC structure and the lattice disorder caused by larger atoms (e.g., Ta and W). For example, the hardness of DED fabricated TiZrNbWMo was 700 HV, and it increased to 1300 HV after annealing at 800 °C for 20 h [68]. In addition, tensile properties of AM MPEAs can also be influenced dramatically by the addition or removal of components. The quinary CoCrFeMnNi produced by PBF exhibited a yield strength of 510 MPa, an ultimate strength of 610 MPa, and an elongation of 36% [142]. In contrast, quaternary MPEAs CoCrFeNi fabricated by using the same AM technique had a yield strength, an ultimate tensile strength and an elongation of 600 MPa, 745 MPa and 32%, respectively [140].

The AM processing parameters play a key role in controlling the microstructure of MPEAs and, hence, their mechanical properties. Lin et al. [109] showed that highly dense (a relative density of 99.71%) FeCoCrNi fabricated by optimized LPBF parameters exhibits superior properties with a yield strength of 600 MPa, ultimate tensile strength of 720 MPa and elongation of 31.85% (Fig. 15b). Xiang et al. [138] demonstrated that an increased yield strength from 189 to 290 MPa can be achieved in DED fabricated

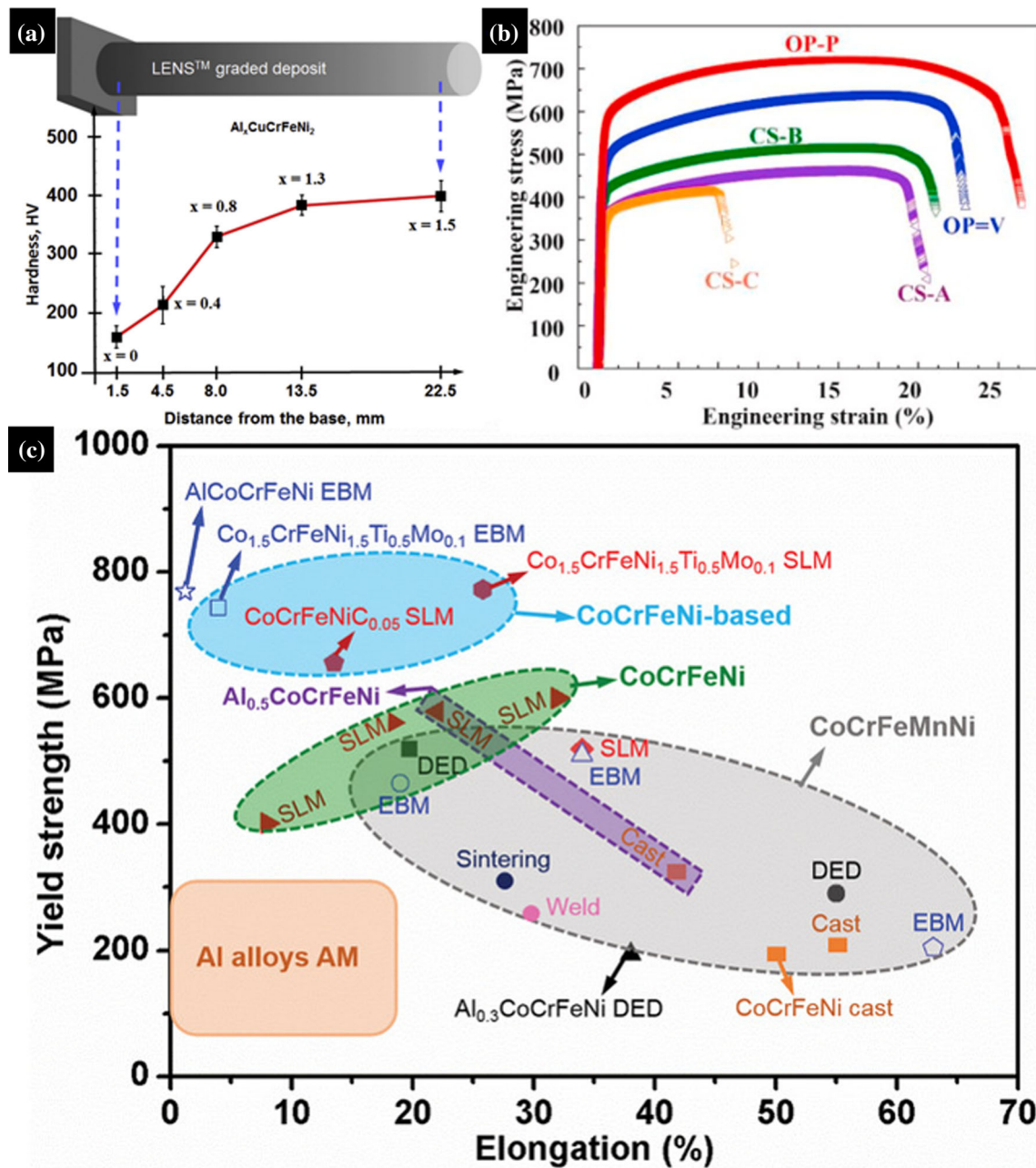


Figure 15 a Variation in Vickers hardness of a compositionally graded DED $\text{Al}_x\text{CrCuFeNi}_2$ [133]. b Stress–strain curves of OP-V, CS-A, CS-B, CS-C, and OP-P, respectively, correspond to a–e in Fig. 2 [109]. c Summary of tensile yield strength and elongation

for AM MPEAs [143]. a Reproduced with permission from Elsevier. [ref. no. 5173970948635] b Reproduced with permission from Elsevier. [ref. no. 5173970060838] c Reproduced with permission from John Wiley and Sons [ref. no. 5173971271338].

CrMnFeCoNi MPEAs through increasing the laser power from 1000 to 1400 W. This was attributed mainly to grain morphology evolution from columnar grains at low laser power to equiaxed grains at high laser power. More heat accumulation at higher laser power promoted a columnar-to-equiaxed

structure transition (CET), which enhanced the strength of the DED fabricated CrMnFeCoNi.

AM induced processing defects in the fabricated MPEA components, such as pores and cracks, can also be a source for fracture and can hence deteriorate the mechanical properties. Hot isostatic pressing (HIP) is commonly used for post-processing of AM

fabricated MPEAs to improve the densification and strength. Li et al. [142] enhanced the densification of a LPBF fabricated CrCoNiFeMn MPEA from 98.2 to 99.1% by HIP, which increased the tensile strength from 601 to 646 MPa. However, the ductility decreased from 35 to 18%. Joseph et al. [77] reported a decrease in elongation around 88% in DED fabricated $Al_xCoCrFeNi$ after HIP. This ductility loss was mainly caused by a transition from ductile fracture to brittle fracture due to precipitation of the σ -phase after HIP. Annealing is another post-AM processing that influences properties of MPEAs by reducing residual stress, altering grain size, and/or reducing chemical segregation. For example, Lin et al. [144] reported the influence of annealing temperature on the mechanical properties of LPBF fabricated FeCoCrNi. Increasing the annealing temperature from 773 to 1573 K can change the yield strength, ultimate tensile strength, and ductility from 581.9 to 221 MPa, 707.9 to 633.2 MPa and 20 to 45%, respectively. A summary of previous studies on the yield strength and elongation of most MPEAs fabricated by different AM technologies is illustrated in Fig. 15 (c) [143]. It can be seen that for MPEAs with an FCC crystal structure, an excellent strength-ductility balance can be achieved with the strength ranging from 200 to 600 MPa and elongation up to 70%. Additionally, by introducing a BCC phase or particles to AM fabricated FCC MPEAs, the strength of the MPEAs can be further increased to around 800 MPa but with some ductility sacrificed at the same time.

Current challenges and future development for AM of MPEAs

Current challenges

MPEA powder feedstock scarcity for AM

Currently, only a limited number of MPEAs, mainly 3d transition metal MPEAs and a few refractory MPEAs, have been successfully fabricated by AM, particularly for PBF [50, 145]. The main reasons are twofold. Firstly, MPEA powders which are suitable for AM are generally difficult to produce via existing metal powder production techniques, e.g., gas-atomization. As for PBF, it has stringent requirements on the size, flowability, and oxygen content as well as other aspects (e.g., surface state) of

the powder feedstock since these characteristics of powders seriously affect the PBF process as well as the microstructure and properties of fabricated MPEAs [146–148]. Additionally, solubility, mixing entropy, and melting point difference between composition elements also need to be considered to avoid liquid phase precipitation or intermetallic compound formation during MPEA powder fabrication [149, 150]. Moreover, the high melting temperature and poor machinability caused by the high strength of refractory MPEAs also make them difficulties in powder production [151, 152]. The MPEAs powders fabricated by atomization methods exhibited high spherical, low oxygen content, and uniform composition [153–155]. However, it is a relatively high cost and low efficiency process. Mechanical alloying, compared with atomization, can conveniently produce MPEA powders with any ratios of elements materials and high solid solubility, but the flowability of powders produced by this method is relatively lower [156]. Thus, producing prealloyed powders for MPEAs with the high solid solubility, homogeneous composition and high spherical degree is a challenging and costly process. Secondly, not all MPEAs are suitable for AM. For instance, intrinsic factors such as high laser reflectivity, high concentration of volatile elements, high thermal conductivity, and/or high melting point can make it difficult to establish optimized AM processing parameters for producing fully dense and crack-free MPEAs [157]. Compared with traditional alloys for AM such as stainless steel, Ti6Al4V, etc., these features of MPEAs can complicate the AM process optimization, which will further pose a challenge to the subsequent microstructure control and properties tailoring for these alloys or even prevent successful manufacturing of any high quality MPEA parts.

Control of processing defects during AM of MPEAs

Although optimized processing parameters can help the densification or bonding process during the AM fabrication process of MPEAs parts, processing defects are still ubiquitous in MPEAs produced by AM [158, 159]. For example, in addition to the defects listed in Sect. 3, MPEA feedstock with high oxygen content could result in high level of porosity in the fabricated MPEA parts, which is mainly attributed to the balling effects and the formation of oxides during solidification [160, 161]. Moreover, due to the

different evaporation rates of elements in MPEAs, the high temperature, and repeated melting and remelting process during AM can also lead to a compositional variation compared with the original powder, in particular when one of the principal elements has a low boiling/evaporation point [157, 162]. This will not only affect the microstructure and properties of the fabricated MPEAs but also influence the certification and qualification of MPEAs parts if demanding industrial applications, such as aerospace, are targeted. Furthermore, the support structure for AM fabricated parts is another critical factor for producing MPEAs with complex geometry. Defective support structure can give rise to an uneven stress distribution which can further cause a severe deformation in the fabricated MPEAs parts during AM, in most cases resulting in the failure of the MPEAs build [163–165]. Thus, optimized process parameters, high flowability and low oxygen content feedstock, gas control during printing and well-designed support structure are the possible actions to reduce defects in MPEAs produced by AM.

Limited understanding of the microstructure evolution in AM fabricated MPEAs

AM, as a class of emerging advanced manufacturing technique, has a unique layer-wise manufacturing process. Some of the key characteristics for AM, such as rapid heating and cooling rates, directional and steep heat flux and thermal gradient, and cyclic heating and cooling generally lead to unique microstructures in AM MPEAs which are different from the microstructures in their counterparts obtained using conventional manufacturing techniques [64, 136, 166]. Although great research effort has been devoted in recent years, the microstructure evolution of AM MPEAs has not been fully understood. For example, the influence of thermal history on the spatial distribution of MPEA elements in the fabricated parts is still unknown. The effect of changing heat flux direction on grains growth in the melt pool of the AM MPEAs is not clear with several proposed mechanisms still under ongoing debate. There is also a lack of understanding of how the minor deviations in composition due to element evaporation during AM will impact the microstructure formation and evolution as well as the phase formation in the fabricated MPEAs. These scientific

questions will need systematic and in-depth research in future to be answered.

Repeatability and reproducibility of AM of MPEAs

AM is a complicated process wherein many machine-related processing parameters (e.g., energy power, scanning speed, hatch space, layer thickness, and scanning strategies) have a huge impact on the fabrication process as well as the microstructure and properties of the MPEAs. Moreover, fluctuations in laser scan speed, variation of mechanical properties (elasticity, friction coefficient, and damping coefficients) of powder particles, variation of diffusion coefficient of the material, uncertainty of absorption coefficient and measurement errors of AM increase the uncertainty of AM. With the added complexity imposed by the presence of multi-principal elements in MPEAs, it becomes even more challenging to obtain satisfactory repeatability and reproducibility of the AM process for these alloys [167–169]. For example, even for MPEA samples manufactured in the same batch within the same PBF machine using the same processing parameters, different microstructures, and properties may arise in the MPEAs. This is probably attributed to multiple reasons including relative position of MPEA parts on the build plate, influence of flowing gas patterns in the build chamber and the irregular splash movement/behavior from melt pools, etc. As such, it will be an important area for future development to improve the robustness of the AM processes and/or systems with the aim to enhance the repeatability and reproducibility of the AM process.

Future prospects and research directions

Design of new MPEAs for AM

Research and applications of AM MPEAs are still in its early stage. Most published works are focused on the 3d transition and refractory metal element MPEAs. New alloy systems/compositions should be explored and developed for AM to further expand the MPEAs materials palette and uncover their potential applications, e.g., lightweight MPEA systems consisting of Li, Mg, Al and Si that can be used in aerospace applications. Additionally, precious metal MPEAs, for example IrOsReRhRu and PdPtCuNiP, have shown excellent catalytic

performance as have HEA composed of lower cost elements such as FeCoNiAlTi [13, 14, 170]. If these MPEAs can be successfully designed and fabricated into complex structures with large surface areas using AM technologies, it is anticipated that related applications will become possible and more value will also be added to their practical applications. To facilitate this alloy design process, computational modeling can be used. Currently, density functional theory (DFT) and molecular dynamics (MD) are widely used in designing new MPEAs with different compositions through the modeling of the phase stability, solidification behavior, and crystallization kinetics of MPEAs, mainly targeting the design of MPEAs with novel or enhanced properties [171, 172]. Once new MPEAs have been designed, the production of high quality prealloyed powder or filament feedstock from these new and novel MPEAs will become another important cornerstone as prerequisite for future research on AM of MPEAs.

Integrated computational materials engineering for AM of MPEAs

Similar to other metals and alloys, many complex physical phenomena such as laser-material interactions, surface tension, and residual stresses, Marangoni flow inside melt pools, melt pool dynamics, phase transitions, and rapid solidification processes with cyclic heating and cooling that occur during the AM process of MPEAs are difficult to analyze and understand only through experiments. Therefore, finite element modeling, molecular dynamics simulation, CALPHAD modeling, and other advanced and high fidelity integrated computational materials engineering (ICME) techniques have also been introduced into the AM field in recent years to help investigate and understand the solidification process, thermal histories, melt pool evolution, processing defect formation, and microstructure formation and properties of AM produced MPEAs and other critical problems mentioned above [173, 174]. Additionally, with the aim to design, qualify, and certify AM fabricated components, there is a current effort to couple computer-aided engineering, digital twins, and internet of things (IoT) with AM to simulate, monitor, and predict the overall microstructure and properties and service performance of AM fabricated components [175, 176]. However, these computational modeling methods and ICME techniques generally

require high quality experimental data, very accurate materials properties and characteristics (e.g., high temperature properties) and substantial computing power as the models become sophisticated with less simplifications. As such, how to obtain the required materials properties, and how to design and develop new and efficient computational models to better represent the real AM processing of MPEAs and at the same time consume less computing power will be one of the critical problems to solve in future.

Machine learning for AM of MPEAs

Machine learning has been recognized as a powerful and effective tool for solving complex problems in many research fields due to its capability of processing and understanding high-dimensional and very large dataset without consuming too much computing power. It is expected that machine learning can also improve the development of AM MPEAs in several ways [177]. Firstly, it can enable the exploration of new MPEAs and the characterization of their solid solution structure and the evaluation of their AM processability by analyzing their physical and chemical properties [178–180]. Secondly, large optimal processing windows for AM of MPEAs can be established by machine learning methods which will allow the tailoring of their microstructures and properties, which has been recently demonstrated for conventional alloys [62, 63]. Thirdly, exploring the relationships between the alloy composition, processing, microstructure, and properties for AM MPEAs would generally require a huge number of experiments, which poses a significant challenge in terms of needed time and resources. In contrast, machine learning models can be established for predicting the process-microstructure-property relationships of many AM MPEAs by using only a limited amount of experimental data [181]. In future, it is expected that a giant database consisting of characteristics of feedstock materials, AM fabrication techniques and process, microstructure information, and various final component properties will be generated with the assistance of machine learning techniques. This database will be able to automatically match materials and AM processes with corresponding design guidelines and methods for manufacturing MPEAs for various industrial applications.

New AM techniques for MPEAs

Compared with traditional manufacturing techniques, various AM technologies have potential advantages in producing MPEAs with either uniform or graded composition, complex geometric shapes, and tailorable local microstructures and hence tailorable properties. Nonetheless, the development of new AM technologies will be desirable in future to further improve the robustness of the AM processes as well as the processability of MPEAs by AM, which will lead to improved quality of the AM fabricated MPEAs. Some small but important advancements such as optimizing the feedstock system in DED technology and inserting a more homogenous pre-heating system in PBF machines can improve the quality of the AM fabricated MPEAs by reducing residual stresses. Other new opportunities including integrating a magnetic, acoustic, or gravitational field into the current AM processes, can also bring new advances in manufacturing high quality MPEAs parts with intricate structures and more functionalities, e.g., changing shape and structure in response to environment stimuli [182, 183].

Conclusion

MPEAs are a class of relatively new engineering materials designed via a novel design concept, i.e., increasing the entropy of mixing of the alloy system. They often form simple phase solid solution structure with large lattice distortion caused by the multiple element composition. As such, MPEAs have potential to deliver excellent properties, such as fatigue performance, high-temperature creep and hydrogen brittleness resistance, corrosion resistance, and radiation resistance that make them attractive for many applications such as turbine components, coatings, catalysts, biomedical devices, and nuclear reactor materials. However, the conventional manufacturing of MPEAs has some drawbacks or limitations such as coarse grains and composition segregation. The layer-wise manufacturing process renders AM an attractive manufacturing technique for the fabrication of MPEAs with complex geometry, unique microstructures, and tailorable properties, which can unlock the potential of MPEAs for different applications. In the past decade, AM MPEAs has received more and more attention from both academia and

industry. However, although promising progress has been made, AM MPEAs research is still in its early stage with many identified challenges. Therefore, this review on AM MPEAs aims to provide insight into the state-of-the-art in the AM MPEA field, with a focus on the microstructure characteristics, mechanical properties, current challenges, and research prospects for AM MPEAs.

It is hoped that this review can arouse interest and stimulate inspiration for more and more researchers to join the collective efforts in the AM MPEAs field. It is anticipated and strongly believed that more and more detailed and comprehensive research studies will be carried out and reported in coming years to promote and accelerate the real application and wide implementation of AM MPEAs for broad industrial sectors.

Acknowledgments

X.L. would like to acknowledge the financial support from Australian Research Council (ARC) Discovery Early Career Researcher Award (DECRA) DE190101495.

Funding

Open Access funding enabled and organized by CAUL and its Member Institutions.

Declarations

Conflict of interest The authors declare that they have no conflict of interest.

Open Access This article is licensed under a Creative Commons Attribution 4.0 International License, which permits use, sharing, adaptation, distribution and reproduction in any medium or format, as long as you give appropriate credit to the original author(s) and the source, provide a link to the Creative Commons licence, and indicate if changes were made. The images or other third party material in this article are included in the article's Creative Commons licence, unless indicated otherwise in a credit line to the material. If material is not included in the article's Creative Commons licence and your intended use is not permitted by statutory regulation or exceeds the permitted use, you will need to obtain permission

directly from the copyright holder. To view a copy of this licence, visit <http://creativecommons.org/licenses/by/4.0/>.

References

- [1] Cantor B, Chang ITH, Knight P, Vincent AJB (2004) Microstructural development in equiatomic multicomponent alloys. *Mater Sci Eng, A* 375–377:213–218. <https://doi.org/10.1016/j.msea.2003.10.257>
- [2] Yeh JW, Chen SK, Lin SJ, Gan JY, Chin TS, Shun TT, Tsau CH, Chang SY (2004) Nanostructured high-entropy alloys with multiple principal elements: novel alloy design concepts and outcomes. *Adv Eng Mater* 6(5):299–303. <http://doi.org/10.1002/adem.2003005672004>
- [3] Yeh J-W (2006) Recent progress in high-entropy alloys. *Annales de Chimie Sci des Matér* 31(6):633–648. <https://doi.org/10.3166/acsm.31.633-648>
- [4] Zhang Y, Wj P (2012) Microstructural control and properties optimization of high-entrop alloys. *Proced Eng* 27:1169–1178. <https://doi.org/10.1016/j.proeng.2011.12.568>
- [5] Ye YF, Wang Q, Lu J, Liu CT, Yang Y (2016) High-entropy alloy: challenges and prospects. *Mater Today* 19(6):349–362. <https://doi.org/10.1016/j.mattod.2015.11.026>
- [6] Yeh J-W, Lin S-J (2018) Breakthrough applications of high-entropy materials. *J Mater Res* 33(19):3129–3137. <https://doi.org/10.1557/jmr.2018.283>
- [7] Reed RC (2008) *The superalloys: fundamentals and applications*. Cambridge University Press
- [8] Tsao TK, Yeh AC, Kuo CM, Kakehi K, Murakami H, Yeh JW, Jian SR (2017) The high temperature tensile and creep behaviors of high entropy superalloy. *Sci Rep* 7(1):12658. <https://doi.org/10.1038/s41598-017-13026-7>
- [9] Padture NP, Gell M, Jordan EH (2002) Thermal barrier coatings for gas-turbine engine applications. *Science* 296(5566):280–284. <https://doi.org/10.1126/science.1068609>
- [10] Yan X, Zhang Y (2020) Functional properties and promising applications of high entropy alloys. *Scripta Mater* 187:188–193. <https://doi.org/10.1016/j.scriptamat.2020.06.017>
- [11] Praveen S, Kim HS (2018) High-entropy alloys: potential candidates for high-temperature applications-an overview. *Adv Eng Mater* 20(1):1700645. <https://doi.org/10.1002/adem.201700645>
- [12] Gao MC, Yeh J-W, Liaw PK, Zhang YJCSIP (2016) *High-entropy alloys*, Springer.
- [13] Jia Z, Yang T, Sun L, Zhao Y, Li W, Luan J, Lyu F, Zhang LC, Kruzic JJ, Kai JJ, Huang JC, Lu J, Liu CT (2020) A novel multinary intermetallic as an active electrocatalyst for hydrogen evolution. *Adv Mater* 32(21):e2000385. <https://doi.org/10.1002/adma.202000385>
- [14] Jia Z, Nomoto K, Wang Q, Kong C, Sun L, Zhang LC, Liang SX, Lu J, Kruzic JJ (2021) A self-supported high-entropy metallic glass with a nanosponge architecture for efficient hydrogen evolution under alkaline and acidic conditions. *Adv Funct Mater* 31(38):2101586. <https://doi.org/10.1002/adfm.202101586>
- [15] Wu Z, Bei H, Pharr GM, George EP (2014) Temperature dependence of the mechanical properties of equiatomic solid solution alloys with face-centered cubic crystal structures. *Acta Mater* 81:428–441. <https://doi.org/10.1016/j.actamat.2014.08.026>
- [16] Miracle DB, Senkov ON (2017) A critical review of high entropy alloys and related concepts. *Acta Mater* 122:448–511. <https://doi.org/10.1016/j.actamat.2016.08.081>
- [17] Coury FG, Zepón G, Bolfarini C (2021) Multi-principal element alloys from the CrCoNi family: outlook and perspectives. *J Market Res* 15:3461–3480. <https://doi.org/10.1016/j.jmrt.2021.09.095>
- [18] Zhang C, Zhang F, Diao H, Gao MC, Tang Z, Poplawsky JD, Liaw PK (2016) Understanding phase stability of Al-Co-Cr-Fe-Ni high entropy alloys. *Mater Des* 109:425–433. <https://doi.org/10.1016/j.matdes.2016.07.073>
- [19] Zhang M, Ma Y, Dong W, Liu X, Lu Y, Zhang Y, Li R, Wang Y, Yu P, Gao Y, Li G (2020) Phase evolution, microstructure, and mechanical behaviors of the CrFe-NiAlxTi medium-entropy alloys. *Mater Sci Eng, A* 771:–138566 <https://doi.org/10.1016/j.msea.2019.138566>
- [20] Chen D, He F, Han B, Wu Q, Tong Y, Zhao Y, Wang Z, Wang J, Kai J-j (2019) Synergistic effect of Ti and Al on L12-phase design in CoCrFeNi-based high entropy alloys. *Intermetallics* 110:106476 <https://doi.org/10.1016/j.intermet.2019.106476>
- [21] Feng X, Utama Surjadi J, Lu Y (2020) Annealing-induced abnormal hardening in nanocrystalline NbMoTaW high-entropy alloy thin films. *Mater Lett* 275:128097 <https://doi.org/10.1016/j.matlet.2020.128097>
- [22] Gubicza J, Heczal A, Kawasaki M, Han J-K, Zhao Y, Xue Y, Huang S, Lábár JL (2019) Evolution of microstructure and hardness in Hf25Nb25Ti25Zr25 high-entropy alloy during high-pressure torsion. *J Alloy Compd* 788:318–328. <https://doi.org/10.1016/j.jallcom.2019.02.220>
- [23] Senkov ON, Wilks GB, Scott JM, Miracle DB (2011) Mechanical properties of Nb25Mo25Ta25W25 and V20Nb20Mo20Ta20W20 refractory high entropy alloys.

- Intermetallics 19(5):698–706. <https://doi.org/10.1016/j.intermet.2011.01.004>
- [24] Youssef KM, Zaddach AJ, Niu C, Irving DL, Koch CC (2014) A novel low-density, high-hardness, high-entropy alloy with close-packed single-phase nanocrystalline structures. *Mater Res Lett* 3(2):95–99. <https://doi.org/10.1080/21663831.2014.985855>
- [25] Torralba JM, Alvaredo P, García-Junceda A (2019) High-entropy alloys fabricated via powder metallurgy. *Crit rev Powder Metall* 62(2):84–114. <https://doi.org/10.1080/00325899.2019.1584454>
- [26] Fu A, Liu B, Xu S, Huang J, Zhang Y, Cao Y, Liu Y (2021) Mechanical properties and microstructural evolution of a novel (FeCoNi)_{86.93}Al_{6.17}Ti_{6.9} medium entropy alloy fabricated via powder metallurgy technique. *J Alloys Compound* 860:158460. <https://doi.org/10.1016/j.jallcom.2020.158460>
- [27] Zheng Y, Jia N, Qian F, Wang J, Xue Y, Jin K (2020) Thermal stability of (CoCrFeNi)₉₄Ti₂Al₄ alloy containing coherent nanoprecipitates at intermediate temperatures. *Materialia* 12:100775. <https://doi.org/10.1016/j.mtla.2020.100775>
- [28] Muniandy Y, He M, Eizadjou M, George EP, Kruzic JJ, Ringer SP, Gludovatz B (2021) Compositional variations in equiatomic CrMnFeCoNi high-entropy alloys. *Mater Charact* 180:111437. <https://doi.org/10.1016/j.matchar.2021.111437>
- [29] Vaidya M, Muralikrishna GM, Murty BS (2019) High-entropy alloys by mechanical alloying: a review. *J Mater Res* 34(5):664–686. <https://doi.org/10.1557/jmr.2019.37>
- [30] Seifi M, Salem A, Beuth J, Harrysson O, Lewandowski JJ (2016) Overview of Materials Qualification Needs for Metal Additive Manufacturing. *Jom* 68(3):747–764. <https://doi.org/10.1007/s11837-015-1810-0>
- [31] Tammis-Williams S, Todd I (2017) Design for additive manufacturing with site-specific properties in metals and alloys. *Scripta Mater* 135:105–110. <https://doi.org/10.1016/j.scriptamat.2016.10.030>
- [32] Ng WL, Chua CK, Shen Y-F (2019) Print me an organ! Why we are not there yet. *Prog Polym Sci* 97:101145. <https://doi.org/10.1016/j.progpolymsci.2019.101145>
- [33] Gu DD, Meiners W, Wissenbach K, Poprawe R (2013) Laser additive manufacturing of metallic components: materials, processes and mechanisms. *Int Mater Rev* 57(3):133–164. <https://doi.org/10.1179/1743280411y.0000000014>
- [34] Murr LE, Martinez E, Amato KN, Gaytan SM, Hernandez J, Ramirez DA, Shindo PW, Medina F, Wicker RB (2012) Fabrication of metal and alloy components by additive manufacturing: examples of 3D materials science. *J Market Res* 1(1):42–54. [https://doi.org/10.1016/s2238-7854\(12\)70009-1](https://doi.org/10.1016/s2238-7854(12)70009-1)
- [35] Frazier WE (2014) Metal additive manufacturing: a review. *J Mater Eng Perform* 23(6):1917–1928. <https://doi.org/10.1007/s11665-014-0958-z>
- [36] Herzog D, Seyda V, Wycisk E, Emmelmann C (2016) Additive manufacturing of metals. *Acta Mater* 117:371–392. <https://doi.org/10.1016/j.actamat.2016.07.019>
- [37] Zhang D, Sun S, Qiu D, Gibson MA, Dargusch MS, Brandt M, Qian M, Easton M (2018) Metal alloys for fusion-based additive manufacturing. *Adv Eng Mater* 20(5):1700952. <https://doi.org/10.1002/adem.201700952>
- [38] Best JP, Ostergaard HE, Li B, Stolpe M, Yang F, Nomoto K, Hasib MT, Muránsky O, Busch R, Li X, Kruzic JJ (2020) Fracture and fatigue behaviour of a laser additive manufactured Zr-based bulk metallic glass. *Addit Manuf* 36:101416. <https://doi.org/10.1016/j.addma.2020.101416>
- [39] Chen W, Yang Q, Huang S, Kruzic JJ, Li X (2021) Compression behavior of graded NiTi Gyroid-structures fabricated by laser powder bed fusion additive manufacturing under monotonic and cyclic loading. *Jom* 73(12):4154–4165. <https://doi.org/10.1007/s11837-021-04938-x>
- [40] Li XP, Roberts MP, O’Keeffe S, Sercombe TB (2016) Selective laser melting of Zr-based bulk metallic glasses: processing, microstructure and mechanical properties. *Mater Des* 112:217–226. <https://doi.org/10.1016/j.matdes.2016.09.071>
- [41] Wang X, Speirs M, Kustov S, Vrancken B, Li X, Kruth J-P, Van Humbeeck J (2018) Selective laser melting produced layer-structured NiTi shape memory alloys with high damping properties and Elinvar effect. *Scripta Mater* 146:246–250. <https://doi.org/10.1016/j.scriptamat.2017.11.047>
- [42] Liu Z, Zhao D, Wang P, Yan M, Yang C, Chen Z, Lu J, Lu Z (2021) Additive manufacturing of metals: microstructure evolution and multistage control. *J Mater Sci Technol* 10-0:224–236. <https://doi.org/10.1016/j.jmst.2021.06.011>
- [43] Dobbstein H, Thiele M, Gurevich EL, George EP, Ostendorf A (2016) Direct metal deposition of refractory high entropy alloy MoNbTaW. *Phys Proced* 83:624–633. <https://doi.org/10.1016/j.phpro.2016.08.065>
- [44] Sing SL, Huang S, Goh GD, Goh GL, Tey CF, Tan JHK, Yeong WY (2021) Emerging metallic systems for additive manufacturing: in-situ alloying and multi-metal processing in laser powder bed fusion. *Prog Mater Sci* 119:100795. <https://doi.org/10.1016/j.pmatsci.2021.100795>
- [45] Gu D, Chen H, Dai D, Ma C, Zhang H, Lin K, Xi L, Zhao T, Hong C, Gasser A, Poprawe R (2020) Carbon nanotubes

- enabled laser 3D printing of high-performance titanium with highly concentrated reinforcement. *iScience* 23(9):101498. <https://doi.org/10.1016/j.isci.2020.101498>
- [46] Fujieda T, Shiratori H, Kuwabara K, Kato T, Yamanaka K, Koizumi Y, Chiba A (2015) First demonstration of promising selective electron beam melting method for utilizing high-entropy alloys as engineering materials. *Mater Lett* 159:12–15. <https://doi.org/10.1016/j.matlet.2015.06.046>
- [47] Shiratori H, Fujieda T, Yamanaka K, Koizumi Y, Kuwabara K, Kato T, Chiba A (2016) Relationship between the microstructure and mechanical properties of an equiatomic AlCoCrFeNi high-entropy alloy fabricated by selective electron beam melting. *Mater Sci Eng, A* 656:39–46. <https://doi.org/10.1016/j.msea.2016.01.019>
- [48] Fujieda T, Shiratori H, Kuwabara K, Hirota M, Kato T, Yamanaka K, Koizumi Y, Chiba A, Watanabe S (2017) CoCrFeNiTi-based high-entropy alloy with superior tensile strength and corrosion resistance achieved by a combination of additive manufacturing using selective electron beam melting and solution treatment. *Mater Lett* 189:148–151. <https://doi.org/10.1016/j.matlet.2016.11.026>
- [49] Brif Y, Thomas M, Todd I (2015) The use of high-entropy alloys in additive manufacturing. *Scripta Mater* 99:93–96. <https://doi.org/10.1016/j.scriptamat.2014.11.037>
- [50] Chen S, Tong Y, Liaw PK (2018) Additive manufacturing of high-entropy alloys: a review. *Entropy (Basel)* 20(12):937. <https://doi.org/10.3390/e20120937>
- [51] Karlsson D, Marshal A, Johansson F, Schuisky M, Sahlberg M, Schneider JM, Jansson U (2019) Elemental segregation in an AlCoCrFeNi high-entropy alloy—a comparison between selective laser melting and induction melting. *J Alloy Compd* 784:195–203. <https://doi.org/10.1016/j.jallcom.2018.12.267>
- [52] Luo S, Gao P, Yu H, Yang J, Wang Z, Zeng X (2019) Selective laser melting of an equiatomic AlCrCuFeNi high-entropy alloy: processability, non-equilibrium microstructure and mechanical behavior. *J Alloy Compd* 771:387–397. <https://doi.org/10.1016/j.jallcom.2018.08.290>
- [53] Luo S, Su Y, Wang Z (2021) Microstructural evolution and mechanisms in additively manufactured AlCrCuFeNi complex concentrated alloys via selective laser melting. *J Alloy Compd* 870:159443. <https://doi.org/10.1016/j.jallcom.2021.159443>
- [54] Zhang M, Zhou X, Wang D, Zhu W, Li J, Zhao YF (2019) AlCoCuFeNi high-entropy alloy with tailored microstructure and outstanding compressive properties fabricated via selective laser melting with heat treatment. *Mater Sci Eng, A* 743:773–784. <https://doi.org/10.1016/j.msea.2018.11.118>
- [55] Zou Y, Ma H, Spolenak R (2015) Ultrastrong ductile and stable high-entropy alloys at small scales. *Nat Commun* 6:7748. <https://doi.org/10.1038/ncomms8748>
- [56] Zhang H, Zhao Y, Huang S, Zhu S, Wang F, Li D (2019) Manufacturing and analysis of high-performance refractory high-entropy alloy via selective laser melting (SLM). *Mater (Basel)* 12(5):720. <https://doi.org/10.3390/ma12050720>
- [57] Johnson L, Mahmoudi M, Zhang B, Seede R, Huang X, Maier JT, Maier HJ, Karaman I, Elwany A, Arróyave R (2019) Assessing printability maps in additive manufacturing of metal alloys. *Acta Mater* 176:199–210. <https://doi.org/10.1016/j.actamat.2019.07.005>
- [58] Kim J, Wakai A, Moridi A (2020) Materials and manufacturing renaissance: additive manufacturing of high-entropy alloys. *J Mater Res* 35(15):1963–1983. <https://doi.org/10.1557/jmr.2020.140>
- [59] Sun K, Peng W, Yang L, Fang L (2020) Effect of SLM processing parameters on microstructures and mechanical properties Al_{0.5}CoCrFeNi high entropy alloys. *Metals* 10(2):292. <https://doi.org/10.3390/met10020292>
- [60] Zhang J, Song B, Wei Q, Bourell D, Shi Y (2019) A review of selective laser melting of aluminum alloys: processing, microstructure, property and developing trends. *J Mater Sci Technol* 35(2):270–284. <https://doi.org/10.1016/j.jmst.2018.09.004>
- [61] Li XP, Ji G, Chen Z, Addad A, Wu Y, Wang HW, Vleugels J, Van Humbeeck J, Kruth JP (2017) Selective laser melting of nano-TiB₂ decorated AlSi10Mg alloy with high fracture strength and ductility. *Acta Mater* 129:183–193. <https://doi.org/10.1016/j.actamat.2017.02.062>
- [62] He P, Liu Q, Kruzic JJ, Li X (2022) Machine-learning assisted additive manufacturing of a TiCN reinforced AlSi10Mg composite with tailorable mechanical properties. *Mater Lett* 307:131018. <https://doi.org/10.1016/j.matlet.2021.131018>
- [63] Liu Q, Wu H, Paul MJ, He P, Peng Z, Gludovatz B, Kruzic JJ, Wang CH, Li X (2020) Machine-learning assisted laser powder bed fusion process optimization for AlSi10Mg: new microstructure description indices and fracture mechanisms. *Acta Mater* 201:316–328. <https://doi.org/10.1016/j.actamat.2020.10.010>
- [64] Cai Y, Shan M, Cui Y, Manladan SM, Lv X, Zhu L, Sun D, Wang T, Han J (2021) Microstructure and properties of FeCoCrNi high entropy alloy produced by laser melting deposition. *J Alloy Compd* 887:161323. <https://doi.org/10.1016/j.jallcom.2021.161323>
- [65] Wang Q, Amar A, Jiang C, Luan H, Zhao S, Zhang H, Le G, Liu X, Wang X, Yang X, Li J (2020) CoCrFeNiMo_{0.2}

- high entropy alloy by laser melting deposition: prospective material for low temperature and corrosion resistant applications. *Intermetallics* 119:106727. <https://doi.org/10.1016/j.intermet.2020.106727>
- [66] Xue P, Zhu L, Xu P, Ren Y, Xin B, Meng G, Yang Z, Liu Z (2021) Research on process optimization and microstructure of CrCoNi medium-entropy alloy formed by laser metal deposition. *Opt Laser Technol* 142:107167. <https://doi.org/10.1016/j.optlastec.2021.107167>
- [67] Zhang H, Pan Y, He Y-Z (2011) Synthesis and characterization of FeCoNiCrCu high-entropy alloy coating by laser cladding. *Mater Des* 32(4):1910–1915. <https://doi.org/10.1016/j.matdes.2010.12.001>
- [68] Zhang M, Zhou X, Yu X, Li J (2017) Synthesis and characterization of refractory TiZrNbWMo high-entropy alloy coating by laser cladding. *Surf Coat Technol* 311:321–329. <https://doi.org/10.1016/j.surfcoat.2017.01.012>
- [69] Ley N, Joshi SS, Zhang B, Ho Y-H, Dahotre NB, Young ML (2018) Laser coating of a CrMoTaWZr complex concentrated alloy onto a H13 tool steel die head. *Surf Coat Technol* 348:150–158. <https://doi.org/10.1016/j.surfcoat.2018.02.038>
- [70] Cai Z, Jin G, Cui X, Liu Z, Zheng W, Li Y, Wang L (2016) Synthesis and microstructure characterization of Ni-Cr-Co-Ti-V-Al high entropy alloy coating on Ti-6Al-4V substrate by laser surface alloying. *Mater Charact* 120:229–233. <https://doi.org/10.1016/j.matchar.2016.09.011>
- [71] Jin G, Cai Z, Guan Y, Cui X, Liu Z, Li Y, Dong M, Zhang D (2018) High temperature wear performance of laser-cladded FeNiCoAlCu high-entropy alloy coating. *Appl Surf Sci* 445:113–122. <https://doi.org/10.1016/j.apsusc.2018.03.135>
- [72] Yue TM, Xie H, Lin X, Yang HO, Meng GH (2014) Solidification behaviour in laser cladding of AlCoCrCu-FeNi high-entropy alloy on magnesium substrates. *J Alloy Compd* 587:588–593. <https://doi.org/10.1016/j.jallcom.2013.10.254>
- [73] Melia MA, Carroll JD, Whetten SR, Esmaeely SN, Locke J, White E, Anderson I, Chandross M, Michael JR, Argibay N, Schindelholz EJ, Kustas AB (2019) Mechanical and Corrosion Properties of Additively Manufactured CoCr-FeMnNi High Entropy Alloy. *Addit Manuf* 29:100833. <https://doi.org/10.1016/j.addma.2019.100833>
- [74] Nartu MSKKY, Alam T, Dasari S, Mantri SA, Gorsse S, Siller H, Dahotre N, Banerjee R (2020) Enhanced tensile yield strength in laser additively manufactured Al0.3CoCrFeNi high entropy alloy. *Materialia* 9:100522. <https://doi.org/10.1016/j.mtla.2019.100522>
- [75] Gwalani B, Gangireddy S, Shukla S, Yannetta CJ, Valentin SG, Mishra RS, Banerjee R (2019) Compositionally graded high entropy alloy with a strong front and ductile back. *Mater Today Commun* 20:100602. <https://doi.org/10.1016/j.mtcomm.2019.100602>
- [76] Qiu Z, Yao C, Feng K, Li Z, Chu PK (2018) Cryogenic deformation mechanism of CrMnFeCoNi high-entropy alloy fabricated by laser additive manufacturing process. *Int J Lightweight Mater Manuf* 1(1):33–39. <https://doi.org/10.1016/j.ijlmm.2018.02.001>
- [77] Joseph J, Jarvis T, Wu X, Stanford N, Hodgson P, Fabijanic DM (2015) Comparative study of the microstructures and mechanical properties of direct laser fabricated and arc-melted Al x CoCrFeNi high entropy alloys. *Mater Sci Eng, A* 633:184–193. <https://doi.org/10.1016/j.msea.2015.02.072>
- [78] Williams SW, Martina F, Addison AC, Ding J, Pardal G, Colegrove P (2016) Wire+arc additive manufacturing. *Mater Sci Technol* 32(7):641–647. <https://doi.org/10.1179/1743284715y.0000000073>
- [79] Zhang Y, Zuo TT, Tang Z, Gao MC, Dahmen KA, Liaw PK, Lu ZP (2014) Microstructures and properties of high-entropy alloys. *Prog Mater Sci* 61:1–93. <https://doi.org/10.1016/j.pmatsci.2013.10.001>
- [80] Zhou YJ, Zhang Y, Kim TN, Chen GL (2008) Microstructure characterizations and strengthening mechanism of multi-principal component AlCoCrFeNiTi0.5 solid solution alloy with excellent mechanical properties. *Mater Lett* 62(17–18):2673–2676. <https://doi.org/10.1016/j.matlet.2008.01.011>
- [81] Wang XF, Zhang Y, Qiao Y, Chen GL (2007) Novel microstructure and properties of multicomponent CoCr-CuFeNiTi_x alloys. *Intermetallics* 15(3):357–362. <https://doi.org/10.1016/j.intermet.2006.08.005>
- [82] Liu S, Zhu H, Peng G, Yin J, Zeng X (2018) Microstructure prediction of selective laser melting AlSi10Mg using finite element analysis. *Mater Des* 142:319–328. <https://doi.org/10.1016/j.matdes.2018.01.022>
- [83] Liu H, Jiang Q, Huo J, Zhang Y, Yang W, Li X (2020) Crystallization in additive manufacturing of metallic glasses: a review. *Addit Manuf* 36:101568. <https://doi.org/10.1016/j.addma.2020.101568>
- [84] Li H, Huang Y, Jiang S, Lu Y, Gao X, Lu X, Ning Z, Sun J (2021) Columnar to equiaxed transition in additively manufactured CoCrFeMnNi high entropy alloy. *Mater Des* 197:109262. <https://doi.org/10.1016/j.matdes.2020.109262>
- [85] Ishimoto T, Ozasa R, Nakano K, Weinmann M, Schnitter C, Stenzel M, Matsugaki A, Nagase T, Matsuzaka T, Todai M, Kim HS, Nakano T (2021) Development of TiNbTaZrMo bio-high entropy alloy (BioHEA) super-solid solution by selective laser melting, and its improved mechanical property and biocompatibility. *Scripta Mater* 194:113658. <https://doi.org/10.1016/j.scriptamat.2020.113658>

- [86] Vikram RJ, Murty BS, Fabijanic D, Suwas S (2020) Insights into micro-mechanical response and texture of the additively manufactured eutectic high entropy alloy. *J Alloys Compd* 827:154032. <https://doi.org/10.1016/j.jallcom.2020.154034>
- [87] Xie Y, Liang J, Zhang D, Luo Y, Zhang Z, Liu Y, Wang J (2020) Sustaining strength–ductility synergy of CoCrFe–NiMn high entropy alloy by a multilevel heterogeneity associated with nanoparticles. *Scripta Mater* 187:390–394. <https://doi.org/10.1016/j.scriptamat.2020.06.054>
- [88] Ansari MJ, Nguyen DS, Park HS (2019) Investigation of SLM process in terms of temperature distribution and melting pool size: modeling and experimental approaches. *Mater (Basel)* 12(8):1272. <https://doi.org/10.3390/ma12081272>
- [89] Zhang C, Li X, Gao M (2020) Effects of circular oscillating beam on heat transfer and melt flow of laser melting pool. *J Market Res* 9(4):9271–9282. <https://doi.org/10.1016/j.jmrt.2020.06.030>
- [90] He P, Webster RF, Yakubov V, Kong H, Yang Q, Huang S, Ferry M, Kruzic JJ, Li X (2021) Fatigue and dynamic aging behavior of a high strength Al-5024 alloy fabricated by laser powder bed fusion additive manufacturing. *Acta Mater* 220:117312. <https://doi.org/10.1016/j.actamat.2021.117312>
- [91] Polonsky AT, Lenthe WC, Echlin MP, Livescu V, Gray GT, Pollock TM (2020) Solidification-driven orientation gradients in additively manufactured stainless steel. *Acta Mater* 183:249–260. <https://doi.org/10.1016/j.actamat.2019.10.047>
- [92] Li H, Huang Y, Sun J, Lu Y (2021) The relationship between thermo-mechanical history, microstructure and mechanical properties in additively manufactured CoCr–FeMnNi high entropy alloy. *J Mater Sci Technol* 77:187–195. <https://doi.org/10.1016/j.jmst.2020.10.052>
- [93] Ikeda T, Yonehara M, Ikeshoji T-T, Nobuki T, Hatate M, Kuwabara K, Otsubo Y, Kyogoku H (2021) Influences of process parameters on the microstructure and mechanical properties of CoCrFeNiTi based high-entropy alloy in a laser powder bed fusion process. *Crystals* 11(5):549. <https://doi.org/10.3390/cryst11050549>
- [94] Peng S, Mooraj S, Feng R, Liu L, Ren J, Liu Y, Kong F, Xiao Z, Zhu C, Liaw PK, Chen W (2021) Additive manufacturing of three-dimensional (3D)-architected CoCrFe–NiMn high-entropy alloy with great energy absorption. *Scripta Mater* 190:46–51. <https://doi.org/10.1016/j.scriptamat.2020.08.028>
- [95] Liu G, Zhang X, Chen X, He Y, Cheng L, Huo M, Yin J, Hao F, Chen S, Wang P, Yi S, Wan L, Mao Z, Chen Z, Wang X, Cao Z, Lu J (2021) Additive manufacturing of structural materials. *Mater Sci Eng R Rep* 145:100596. <https://doi.org/10.1016/j.mser.2020.100596>
- [96] Zhao YL, Yang T, Zhu JH, Chen D, Yang Y, Hu A, Liu CT, Kai JJ (2018) Development of high-strength Co-free high-entropy alloys hardened by nanosized precipitates. *Scripta Mater* 148:51–55. <https://doi.org/10.1016/j.scriptamat.2018.01.028>
- [97] Colosimo BM, Grasso, M (2016) In-situ monitoring of metal additive manufacturing processes: Sensing and intelligent data analysis. 14th IMEKO TC10 Workshop on Technical Diagnostics 2016: New Perspectives in Measurements, Tools and Techniques for Systems Reliability, Maintainability and Safety, pp. 248–253
- [98] Grasso M, Laguzza V, Semeraro Q, Colosimo B (2016) In-process monitoring of selective laser melting: spatial detection of defects via image data analysis. *J Manuf Sci Eng* 139:051001–051001. <https://doi.org/10.1115/1.4034715>
- [99] Guo J, Goh M, Zhu Z, Lee X, Nai MLS, Wei J (2018) On the machining of selective laser melting CoCrFeMnNi high-entropy alloy. *Mater Des* 153:211–220. <https://doi.org/10.1016/j.matdes.2018.05.012>
- [100] Sun Z, Tan XP, Descoins M, Mangelinck D, Tor SB, Lim CS (2019) Revealing hot tearing mechanism for an additively manufactured high-entropy alloy via selective laser melting. *Scripta Mater* 168:129–133. <https://doi.org/10.1016/j.scriptamat.2019.04.036>
- [101] Chen P, Li S, Zhou Y, Yan M, Attallah MM (2020) Fabricating CoCrFeMnNi high entropy alloy via selective laser melting in-situ alloying. *J Mater Sci Technol* 43:40–43. <https://doi.org/10.1016/j.jmst.2020.01.002>
- [102] Zhou L, Pan H, Hyer H, Park S, Bai Y, McWilliams B, Cho K, Sohn Y (2019) Microstructure and tensile property of a novel AlZnMgScZr alloy additively manufactured by gas atomization and laser powder bed fusion. *Scripta Mater* 158:24–28. <https://doi.org/10.1016/j.scriptamat.2018.08.025>
- [103] Li G, Brodu E, Soete J, Wei H, Liu T, Yang T, Liao W, Vanmeensel K (2021) Exploiting the rapid solidification potential of laser powder bed fusion in high strength and crack-free Al–Cu–Mg–Mn–Zr alloys. *Addit Manuf* 47:102–210 <https://doi.org/10.1016/j.addma.2021.102210>
- [104] Ren Y, Liang L, Shan Q, Cai A, Du J, Huang Q, Liu S, Yang X, Tian Y, Wu H (2020) Effect of volumetric energy density on microstructure and tribological properties of FeCoNiCuAl high-entropy alloy produced by laser powder bed fusion. *Virtual Phys Prototyp* 15(sup1):543–554. <https://doi.org/10.1080/17452759.2020.1848284>
- [105] Kuzminova Y, Firsov D, Dudin A, Sergeev S, Zhilyaev A, Dyakov A, Chupeeva A, Alekseev A, Martynov D,

- Akhatov I, Evlashin S (2020) The effect of the parameters of the powder bed fusion process on the microstructure and mechanical properties of CrFeCoNi medium-entropy alloys. *Intermetallics* 116:106651 <https://doi.org/10.1016/j.intermet.2019.106651>
- [106] Niu P, Li R, Zhu S, Wang M, Chen C, Yuan T (2020) Hot cracking, crystal orientation and compressive strength of an equimolar CoCrFeMnNi high-entropy alloy printed by selective laser melting. *Opt Laser Technol* 127:106147. <https://doi.org/10.1016/j.optlastec.2020.106147>
- [107] Niu PD, Li RD, Yuan TC, Zhu SY, Chen C, Wang MB, Huang L (2019) Microstructures and properties of an equimolar AlCoCrFeNi high entropy alloy printed by selective laser melting. *Intermetallics* 104:24–32. <https://doi.org/10.1016/j.intermet.2018.10.018>
- [108] Ren J, Mahajan C, Liu L, Follette D, Chen W, Mukherjee S (2019) Corrosion behavior of selectively laser melted CoCrFeMnNi high entropy alloy. *Metals* 9(10):1029. <https://doi.org/10.3390/met9101029>
- [109] Lin D, Xu L, Han Y, Zhang Y, Jing H, Zhao L, Minami F (2020) Structure and mechanical properties of a FeCoCrNi high-entropy alloy fabricated via selective laser melting. *Intermetallics* 127:106963. <https://doi.org/10.1016/j.intermet.2020.106963>
- [110] Zhou YH, Zhang ZH, Wang YP, Liu G, Zhou SY, Li YL, Shen J, Yan M (2019) Selective laser melting of typical metallic materials: an effective process prediction model developed by energy absorption and consumption analysis. *Addit Manuf* 25:204–217. <https://doi.org/10.1016/j.addma.2018.10.046>
- [111] Xiang S, Luan H, Wu J, Yao K-F, Li J, Liu X, Tian Y, Mao W, Bai H, Le G, Li Q (2019) Microstructures and mechanical properties of CrMnFeCoNi high entropy alloys fabricated using laser metal deposition technique. *J Alloy Compd* 773:387–392. <https://doi.org/10.1016/j.jallcom.2018.09.235>
- [112] Sistla HR, Newkirk JW, Frank Liou F (2015) Effect of Al/Ni ratio, heat treatment on phase transformations and microstructure of Al_xFeCoCrNi_{2-x} (x=0.3, 1) high entropy alloys. *Mater Des* 81:113–121. <https://doi.org/10.1016/j.matdes.2015.05.027>
- [113] Dobbstein H, Gurevich EL, George EP, Ostendorf A, Laplanche G (2019) Laser metal deposition of compositionally graded TiZrNbTa refractory high-entropy alloys using elemental powder blends. *Addit Manuf* 25:252–262. <https://doi.org/10.1016/j.addma.2018.10.042>
- [114] Dada M, Popoola P, Mathe N, Pityana S, Adeosun S, Aramide O, Lengopeng T (2020) Process optimization of high entropy alloys by laser additive manufacturing. *Eng Rep* 2(10):e12252. <https://doi.org/10.1002/eng2.12252>
- [115] Wu W, Song M, Ni S, Wang J, Liu Y, Liu B, Liao X (2017) Dual mechanisms of grain refinement in a FeCoCrNi high-entropy alloy processed by high-pressure torsion. *Sci Rep* 7:46720. <https://doi.org/10.1038/srep46720>
- [116] Guo S, Ng C, Wang Z, Liu CT (2014) Solid solutioning in equiatomic alloys: limit set by topological instability. *J Alloy Compd* 583:410–413. <https://doi.org/10.1016/j.jallcom.2013.08.213>
- [117] Shun T-T, Chang L-Y, Shiu M-H (2012) Microstructure and mechanical properties of multiprincipal component CoCrFeNiMox alloys. *Mater Charact* 70:63–67. <https://doi.org/10.1016/j.matchar.2012.05.005>
- [118] Wang W-R, Wang W-L, Wang S-C, Tsai Y-C, Lai C-H, Yeh J-W (2012) Effects of Al addition on the microstructure and mechanical property of Al_xCoCrFeNi high-entropy alloys. *Intermetallics* 26:44–51. <https://doi.org/10.1016/j.intermet.2012.03.005>
- [119] Pauly S, Wang P, Kühn U, Kosiba K (2018) Experimental determination of cooling rates in selectively laser-melted eutectic Al-33Cu. *Addit Manuf* 22:753–757. <https://doi.org/10.1016/j.addma.2018.05.034>
- [120] Sun Z, Tan X, Wang C, Descoins M, Mangelinck D, Tor SB, Jäggle EA, Zaeferrer S, Raabe D (2021) Reducing hot tearing by grain boundary segregation engineering in additive manufacturing: example of an Al_xCoCrFeNi high-entropy alloy. *Acta Mater* 204:116505 <https://doi.org/10.1016/j.actamat.2020.116505>
- [121] Li J, Luan H, Zhou L, Amar A, Li R, Huang L, Liu X, Le G, Wang X, Wu J, Jiang C (2020) Phase transformation-induced strengthening of an additively manufactured multiprincipal element CrMnFeCoNi alloy. *Mater Des* 195:108999 <https://doi.org/10.1016/j.matdes.2020.108999>
- [122] Piglion A, Dovgvy B, Liu C, Gourlay CM, Hooper PA, Pham MS (2018) Printability and microstructure of the CoCrFeMnNi high-entropy alloy fabricated by laser powder bed fusion. *Mater Lett* 224:22–25. <https://doi.org/10.1016/j.matlet.2018.04.052>
- [123] Oliveira JP, LaLonde AD, Ma J (2020) Processing parameters in laser powder bed fusion metal additive manufacturing. *Mater Des* 193:108762. <https://doi.org/10.1016/j.matdes.2020.108762>
- [124] Tong Z, Ren X, Jiao J, Zhou W, Ren Y, Ye Y, Larson EA, Gu J (2019) Laser additive manufacturing of FeCrCoMnNi high-entropy alloy: effect of heat treatment on microstructure, residual stress and mechanical property. *J Alloy Compd* 785:1144–1159. <https://doi.org/10.1016/j.jallcom.2019.01.213>
- [125] Zhu ZG, An XH, Lu WJ, Li ZM, Ng FL, Liao XZ, Ramamurty U, Nai SML, Wei J (2019) Selective laser melting enabling the hierarchically heterogeneous

- microstructure and excellent mechanical properties in an interstitial solute strengthened high entropy alloy. *Mater Res Lett* 7(11):453–459. <https://doi.org/10.1080/21663831.2019.1650131>
- [126] Jin M, Piglione A, Dovgvy B, Hosseini E, Hooper PA, Holdsworth SR, Pham M-S (2020) Cyclic plasticity and fatigue damage of CrMnFeCoNi high entropy alloy fabricated by laser powder-bed fusion. *Addit Manuf* 36:101584. <https://doi.org/10.1016/j.addma.2020.101584>
- [127] Yang X, Ge Y, Lehtonen J, Hannula SP (2020) Hierarchical microstructure of laser powder bed fusion produced face-centered-cubic-structured equiatomic CrFeNiMn multi-component alloy. *Mater (Basel)* 13(20):4498. <https://doi.org/10.3390/ma13204498>
- [128] Chew Y, Bi GJ, Zhu ZG, Ng FL, Weng F, Liu SB, Nai SML, Lee BY (2019) Microstructure and enhanced strength of laser aided additive manufactured CoCrFeNiMn high entropy alloy. *Mater Sci Eng, A* 744:137–144. <https://doi.org/10.1016/j.msea.2018.12.005>
- [129] Li X (2018) Additive manufacturing of advanced multi-component alloys: bulk metallic glasses and high entropy alloys. *Adv Eng Mater* 20(5):1700874. <https://doi.org/10.1002/adem.201700874>
- [130] Kuzminova YO, Firsov DG, Dagesyan SA, Konev SD, Sergeev SN, Zhilyaev AP, Kawasaki M, Akhatov IS, Evlashin SA (2021) Fatigue behavior of additive manufactured CrFeCoNi medium-entropy alloy. *J Alloy Compd* 863:158609 <https://doi.org/10.1016/j.jallcom.2021.158609>
- [131] Park JM, Choe J, Park HK, Son S, Jung J, Kim T-S, Yu J-H, Kim JG, Kim HS (2020) Synergetic strengthening of additively manufactured (CoCrFeMnNi)₉₉C₁ high-entropy alloy by heterogeneous anisotropic microstructure. *Addit Manuf* 35:101333 <https://doi.org/10.1016/j.addma.2020.101333>
- [132] Dovgvy B, Piglione A, Hooper PA, Pham M-S (2020) Comprehensive assessment of the printability of CoNiCrFeMn in laser powder bed fusion. *Mater Des* 194:108845. <https://doi.org/10.1016/j.matdes.2020.108845>
- [133] Borkar T, Gwalani B, Choudhuri D, Mikler CV, Yannetta CJ, Chen X, Ramanujan RV, Styles MJ, Gibson MA, Banerjee R (2016) A combinatorial assessment of Al_xCrCuFeNi₂ (0 < x < 1.5) complex concentrated alloys: microstructure, microhardness, and magnetic properties. *Acta Mater* 116:63–76. <https://doi.org/10.1016/j.actamat.2016.06.025>
- [134] Dobbelsstein H, Gurevich EL, George EP, Ostendorf A, Laplanche G (2018) Laser metal deposition of a refractory TiZrNbHfTa high-entropy alloy. *Addit Manuf* 24:386–390. <https://doi.org/10.1016/j.addma.2018.10.008>
- [135] Zhang J, Liu Y, Bayat M, Tan Q, Yin Y, Fan Z, Liu S, Hattel JH, Dargusch M, Zhang M-X (2021) Achieving high ductility in a selectively laser melted commercial pure-titanium via in-situ grain refinement. *Scripta Mater* 191:155–160. <https://doi.org/10.1016/j.scriptamat.2020.09.023>
- [136] Wang H, Zhu ZG, Chen H, Wang AG, Liu JQ, Liu HW, Zheng RK, Nai SML, Primig S, Babu SS, Ringer SP, Liao XZ (2020) Effect of cyclic rapid thermal loadings on the microstructural evolution of a CrMnFeCoNi high-entropy alloy manufactured by selective laser melting. *Acta Mater* 196:609–625. <https://doi.org/10.1016/j.actamat.2020.07.006>
- [137] Wang H, Zhu ZG, Chen HS, Nai SM, An XH, Zheng RK, Primig S, Ringer SP, Liao XZ (2019) Effect of cyclic thermal loadings on the microstructural evolution of a cantor alloy in 3D printing processes. *Microsc Microanal* 25(S2):2568–2569. <https://doi.org/10.1017/s1431927619013576>
- [138] Xiang S, Li J, Luan H, Amar A, Lu S, Li K, Zhang L, Liu X, Le G, Wang X, Qu F, Zhang W, Wang D, Li Q (2019) Effects of process parameters on microstructures and tensile properties of laser melting deposited CrMnFeCoNi high entropy alloys. *Mater Sci Eng, A* 743:412–417. <https://doi.org/10.1016/j.msea.2018.11.110>
- [139] Basu I, De Hosson JTM (2020) Strengthening mechanisms in high entropy alloys: fundamental issues. *Scripta Mater* 187:148–156. <https://doi.org/10.1016/j.scriptamat.2020.06.019>
- [140] Lin D, Xu L, Jing H, Han Y, Zhao L, Zhang Y, Li H (2020) A strong, ductile, high-entropy FeCoCrNi alloy with fine grains fabricated via additive manufacturing and a single cold deformation and annealing cycle. *Addit Manuf* 36:101591. <https://doi.org/10.1016/j.addma.2020.101591>
- [141] Zhou R, Liu Y, Liu B, Li J, Fang Q (2019) Precipitation behavior of selective laser melted FeCoCrNiC_{0.05} high entropy alloy. *Intermetallics* 106:20–25. <https://doi.org/10.1016/j.intermet.2018.12.001>
- [142] Li R, Niu P, Yuan T, Cao P, Chen C, Zhou K (2018) Selective laser melting of an equiatomic CoCrFeMnNi high-entropy alloy: processability, non-equilibrium microstructure and mechanical property. *J Alloy Compd* 746:125–134. <https://doi.org/10.1016/j.jallcom.2018.02.298>
- [143] Han C, Fang Q, Shi Y, Tor SB, Chua CK, Zhou K (2020) Recent advances on high-entropy alloys for 3D printing. *Adv Mater* 32(26):e1903855. <https://doi.org/10.1002/adma.201903855>
- [144] Lin D, Xu L, Jing H, Han Y, Zhao L, Minami F (2020) Effects of annealing on the structure and mechanical

- properties of FeCoCrNi high-entropy alloy fabricated via selective laser melting. *Addit Manuf* 32:101058. <https://doi.org/10.1016/j.addma.2020.101058>
- [145] Ostovari Moghaddam A, Shaburova NA, Samodurova MN, Abdollahzadeh A, Trofimov EA (2021) Additive manufacturing of high entropy alloys: a practical review. *J Mater Sci Technol* 77:131–162. <https://doi.org/10.1016/j.jmst.2020.11.029>
- [146] Anderson IE, White EMH, Dehoff R (2018) Feedstock powder processing research needs for additive manufacturing development. *Curr Opin Solid State Mater Sci* 22(1):8–15. <https://doi.org/10.1016/j.cossms.2018.01.002>
- [147] Snow Z, Martukanitz R, Joshi S (2019) On the development of powder spreadability metrics and feedstock requirements for powder bed fusion additive manufacturing. *Addit Manuf* 28:78–86. <https://doi.org/10.1016/j.addma.2019.04.017>
- [148] Tan JH, Wong WLE, Dalgarno KW (2017) An overview of powder granulometry on feedstock and part performance in the selective laser melting process. *Addit Manuf* 18:228–255. <https://doi.org/10.1016/j.addma.2017.10.011>
- [149] Wang P, Huang P, Ng FL, Sin WJ, Lu S, Nai MLS, Dong Z, Wei J (2019) Additively manufactured CoCrFeNiMn high-entropy alloy via pre-alloyed powder. *Mater Des* 168:107576. <https://doi.org/10.1016/j.matdes.2018.107576>
- [150] Popov VV, Katz-Demyanetz A, Koptyug A, Bamberger M (2019) Selective electron beam melting of Al_{0.5}CrMoNb-Ta_{0.5}high entropy alloys using elemental powder blend. *Heliyon* 5(2):e01188. <https://doi.org/10.1016/j.heliyon.2019.e01188>
- [151] Kang B, Lee J, Ryu HJ, Hong SH (2018) Ultra-high strength WNbMoTaV high-entropy alloys with fine grain structure fabricated by powder metallurgical process. *Mater Sci Eng, A* 712:616–624. <https://doi.org/10.1016/j.msea.2017.12.021>
- [152] Long Y, Su K, Zhang J, Liang X, Peng H, Li X (2018) Enhanced strength of a mechanical alloyed NbMoTaWVTi refractory high entropy alloy. *Materials* 11(5):669. <https://doi.org/10.3390/ma11050669>
- [153] Eißmann N, Klöden B, Weißgärber T, Kieback B (2017) High-entropy alloy CoCrFeMnNi produced by powder metallurgy. *Powder Metall* 60(3):184–197. <https://doi.org/10.1080/00325899.2017.1318480>
- [154] Liu B, Wang J, Liu Y, Fang Q, Wu Y, Chen S, Liu CT (2016) Microstructure and mechanical properties of equimolar FeCoCrNi high entropy alloy prepared via powder extrusion. *Intermetallics* 75:25–30. <https://doi.org/10.1016/j.intermet.2016.05.006>
- [155] Liu Y, Wang J, Fang Q, Liu B, Wu Y, Chen S (2016) Preparation of superfine-grained high entropy alloy by spark plasma sintering gas atomized powder. *Intermetallics* 68:16–22. <https://doi.org/10.1016/j.intermet.2015.08.012>
- [156] Joo SH, Kato H, Jang MJ, Moon J, Kim EB, Hong SJ, Kim HS (2017) Structure and properties of ultrafine-grained CoCrFeMnNi high-entropy alloys produced by mechanical alloying and spark plasma sintering. *J Alloy Compd* 698:591–604. <https://doi.org/10.1016/j.jallcom.2016.12.010>
- [157] Niu P, Li R, Gan K, Yuan T, Xie S, Chen C (2021) Microstructure, properties, and metallurgical defects of an equimolar CoCrNi medium entropy alloy additively manufactured by selective laser melting. *Metall and Mater Trans A* 52(2):753–766. <https://doi.org/10.1007/s11661-020-06121-4>
- [158] Wu B, Pan Z, Ding D, Cuiuri D, Li H, Xu J, Norrish J (2018) A review of the wire arc additive manufacturing of metals: properties, defects and quality improvement. *J Manuf Process* 35:127–139. <https://doi.org/10.1016/j.jmpro.2018.08.001>
- [159] Sanaei N, Fatemi A, Phan N (2019) Defect characteristics and analysis of their variability in metal L-PBF additive manufacturing. *Mater Des* 182:108091. <https://doi.org/10.1016/j.matdes.2019.108091>
- [160] Leung CLA, Marussi S, Towrie M, Atwood RC, Withers PJ, Lee PD (2019) The effect of powder oxidation on defect formation in laser additive manufacturing. *Acta Mater* 166:294–305. <https://doi.org/10.1016/j.actamat.2018.12.027>
- [161] Sun Y, Aindow M, Hebert RJ (2017) The effect of recycling on the oxygen distribution in Ti-6Al-4V powder for additive manufacturing. *Mater High Temp* 35(1–3):217–224. <https://doi.org/10.1080/09603409.2017.1389133>
- [162] Chen W, Yang Q, Huang S, Huang S, Kruzic JJ, Li X (2021) Laser power modulated microstructure evolution, phase transformation and mechanical properties in NiTi fabricated by laser powder bed fusion. *J Alloy Compd* 861:157959. <https://doi.org/10.1016/j.jallcom.2020.157959>
- [163] Cheng L, Liang X, Bai J, Chen Q, Lemon J, To A (2019) On utilizing topology optimization to design support structure to prevent residual stress induced build failure in laser powder bed metal additive manufacturing. *Addit Manuf* 27:290–304. <https://doi.org/10.1016/j.addma.2019.03.001>
- [164] Hussein A, Hao L, Yan C, Everson R, Young P (2013) Advanced lattice support structures for metal additive manufacturing. *J Mater Process Technol* 213(7):1019–1026. <https://doi.org/10.1016/j.jmatprotec.2013.01.020>

- [165] Morgan D, Agba E, Hill C (2017) Support structure development and initial results for metal powder bed fusion additive manufacturing. *Procedia Manuf* 10:819–830. <https://doi.org/10.1016/j.promfg.2017.07.083>
- [166] Pegues JW, Melia MA, Puckett R, Whetten SR, Argibay N, Kustas AB (2021) Exploring additive manufacturing as a high-throughput screening tool for multiphase high entropy alloys. *Addit Manuf* 37:101598. <https://doi.org/10.1016/j.addma.2020.101598>
- [167] Hu Z, Mahadevan S (2017) Uncertainty quantification in prediction of material properties during additive manufacturing. *Scripta Mater* 135:135–140. <https://doi.org/10.1016/j.scriptamat.2016.10.014>
- [168] Wang X, Xiong W (2020) Uncertainty quantification and composition optimization for alloy additive manufacturing through a CALPHAD-based ICME framework. *npj Comput Mater* 6(1):1–11. <https://doi.org/10.1038/s41524-020-00454-9>
- [169] Fabro AT, Meng H, Chronopoulos D (2020) Uncertainties in the attenuation performance of a multi-frequency metastructure from additive manufacturing. *Mech Syst Signal Process* 138:106557. <https://doi.org/10.1016/j.ymsp.2019.106557>
- [170] Yusenkov KV, Riva S, Carvalho PA, Yusenkov MV, Arnaboldi S, Sukhikh AS, Hanfland M, Gromilov SA (2017) First hexagonal close packed high-entropy alloy with outstanding stability under extreme conditions and electrocatalytic activity for methanol oxidation. *Scripta Mater* 138:22–27. <https://doi.org/10.1016/j.scriptamat.2017.05.022>
- [171] Sharma A, Deshmukh SA, Liaw PK, Balasubramanian G (2017) Crystallization kinetics in Al_xCrCoFeNi (0 ≤ x ≤ 40) high-entropy alloys. *Scripta Mater* 141:54–57. <https://doi.org/10.1016/j.scriptamat.2017.07.024>
- [172] Sun X, Zhang H, Lu S, Ding X, Wang Y, Vitos L (2017) Phase selection rule for Al-doped CrMnFeCoNi high-entropy alloys from first-principles. *Acta Mater* 140:366–374. <https://doi.org/10.1016/j.actamat.2017.08.045>
- [173] Lindgren L-E, Lundbäck A, Fisk M, Pederson R, Andersson J (2016) Simulation of additive manufacturing using coupled constitutive and microstructure models. *Addit Manuf* 12:144–158. <https://doi.org/10.1016/j.addma.2016.05.005>
- [174] Cook PS, Murphy AB (2020) Simulation of melt pool behaviour during additive manufacturing: underlying physics and progress. *Addit Manuf* 31:100909. <https://doi.org/10.1016/j.addma.2019.100909>
- [175] Katiyar NK, Goel G, Goel S (2021) Emergence of machine learning in the development of high entropy alloy and their prospects in advanced engineering applications. *Emerg Mater* 4:1635–1648. <https://doi.org/10.1007/s42247-021-00249-8>
- [176] Wang WY, Tang B, Lin D, Zou C, Zhang Y, Shang S-L, Guan Q, Gao J, Fan L, Kou H, Song H, Ma J, Hui X-D, Gao MC, Liu Z-K, Li J (2020) A brief review of data-driven ICME for intelligently discovering advanced structural metal materials: insight into atomic and electronic building blocks. *J Mater Res* 35(8):872–889. <https://doi.org/10.1557/jmr.2020.43>
- [177] Jafary-Zadeh M, Khoo KH, Laskowski R, Branicio PS, Shapeev AV (2019) Applying a machine learning interatomic potential to unravel the effects of local lattice distortion on the elastic properties of multi-principal element alloys. *J Alloy Compd* 803:1054–1062. <https://doi.org/10.1016/j.jallcom.2019.06.318>
- [178] Krishna YV, Jaiswal UK, RM R (2021) Machine learning approach to predict new multiphase high entropy alloys. *Scripta Mater* 197:113804. <https://doi.org/10.1016/j.scriptamat.2021.113804>
- [179] Zhou Z, Zhou Y, He Q, Ding Z, Li F, Yang Y (2019) Machine learning guided appraisal and exploration of phase design for high entropy alloys. *npj Comput Mater* 5(1):1–9. <https://doi.org/10.1038/s41524-019-0265-1>
- [180] Wen C, Zhang Y, Wang C, Xue D, Bai Y, Antonov S, Dai L, Lookman T, Su Y (2019) Machine learning assisted design of high entropy alloys with desired property. *Acta Mater* 170:109–117. <https://doi.org/10.1016/j.actamat.2019.03.010>
- [181] Li L, Xie B, Fang Q, Li J (2021) Machine learning approach to design high entropy alloys with heterogeneous grain structures. *Metall Mater Trans A* 52(2):439–448. <https://doi.org/10.1007/s11661-020-06099-z>
- [182] Kuang X, Roach DJ, Wu J, Hamel CM, Ding Z, Wang T, Dunn ML, Qi HJ (2019) Advances in 4D printing: materials and applications. *Adv Func Mater* 29(2):1805290. <https://doi.org/10.1002/adfm.201805290>
- [183] Chen X, Liu X, Ouyang M, Chen J, Taiwo O, Xia Y, Childs PRN, Brandon NP, Wu B (2019) Multi-metal 4D printing with a desktop electrochemical 3D printer. *Sci Rep* 9(1):3973. <https://doi.org/10.1038/s41598-019-40774-5>

Publisher's Note Springer Nature remains neutral with regard to jurisdictional claims in published maps and institutional affiliations.